CONCENTRATED FERROFLUID EMULSIONS UNDER SHEAR FLOW AND UNIFORM MAGNETIC FIELDS

Raysa Gomes dos Santos

Master's Dissertation

Mechanical Sciences

UNIVERSIDADE DE BRASÍLIA

Faculdade de Tecnologia

Departamento de Engenharia Mecânica

UNIVERSITY OF BRASILIA
FACULTY OF TECHNOLOGY
DEPARTMENT OF MECHANICAL ENGINEERING

CONCENTRATED FERROFLUID EMULSIONS UNDER SHEAR FLOW AND UNIFORM MAGNETIC FIELDS

Raysa Gomes dos Santos

Advisor: Taygoara Felamingo de Oliveira, Ph.D. (ENM/UnB)
Co-advisor: Lucas H. P. da Cunha, Ph.D. (ISMSM/GU)

MASTER'S DISSERTATION

Brasília/DF, July 2024

UNIVERSIDADE DE BRASÍLIA
FACULDADE DE TECNOLOGIA
DEPARTAMENTO DE ENGENHARIA MECÂNICA

Emulsões concentradas de ferrofluido sob fluxo de cisalhamento e campos magnéticos uniformes

Raysa Gomes dos Santos

Dissertação submetida ao Departamento de Engenharia Mecânica como requisito parcial para obtenção do título de Mestre em Ciências Mecânicas.

Banca Examinadora:

Taygoara Felamingo de Oliveira, Ph.D. (ENM/UnB)
Orientador

Lucas Hildebrand Pires da Cunha, Ph.D. (ISMSM/GU)
Coorientador

Yuri Dumaresq Sobral, Ph.D. (MAT/IE/UNB)
Examinador Interno

Ivan Rosa de Siqueira, Ph.D. (DEM/PUC-Rio)
Examinador Externo

Adriano Possebon Rosa, Ph.D. (ENM/UnB)
Suplente

Brasília, 17 de Julho de 2024.

FICHA CATALOGRÁFICA

Santos, Raysa Gomes

Concentrated ferrofluid emulsions under shear flow and uniform magnetic fields. Raysa Gomes dos Santos — Brasília, Julho 2024

66p., 297mm (ENM/FT/UnB, Mestre, Ciências Mecânicas, 2024)

Orientador: Prof. Taygoara Felamingo de Oliveira, PhD. Coorientador: Lucas Hildebrand Pires da Cunha, PhD

Dissertação de Mestrado – Universidade de Brasília

Faculdade de Tecnologia – Julho 2024

Magnetic emulsion, concentrated emulsion, simple shear, level set method

Abstract

This work investigates the response of semidilute magnetic emulsion subjected to simple shear flows and a uniform external magnetic field. Our analysis employs a three-dimensional numerical domain where monodisperse ferrofluid droplets are randomly suspended in a non-magnetic Newtonian carrier fluid. The incompressible Navier-Stokes equations are solved using a second-order projection method. Moreover, we use the level set method to capture the interface and, assuming the droplet surfaces are free of surfactants, implement a repulsive force between droplets to avoid coalescence. We set different droplet concentrations, capillary numbers, and magnetic capillary numbers. First, in the absence of a magnetic field, we determine the effective viscosity for different droplet concentrations and shear rates, obtaining results that agree well with previous works. Later, we observed that the deformation and inclination angle of the droplets increase with the magnetic capillary number, while they decrease when the volume fraction increases. The droplet inclination angle is the angle between its main axis and the main flow direction (x-direction). We found that droplet-droplet interactions can significantly change the dynamics and droplet geometry, leading to a dynamic response. These geometrical changes cause variations in both viscosity and bulk magnetization. As the magnetic capillary number and volume fraction increase, both properties rise. However, when normalized by volume fraction, we observed that droplets in dilute regimes contribute more significantly to these bulk properties. Despite the superparamagnetic hypothesis for magnetic droplets, we compute an misalignment angle between the magnetization and the external magnetic field, which results in torques exerted on the droplets. At low magnetic capillary numbers, an increase in droplet concentration leads to a decrease in this angle. In contrast, the angle increases for higher concentrations. Overall, we investigated the effects that the presence of multiple ferrofluid droplets has on the bulk properties of the emulsion.

Key-words: magnetic emulsion, concentrated emulsion, simple shear, level set method

Resumo

Este trabalho investiga a resposta de uma emulsão magnética semidiluída sujeita a fluxos de cisalhamento simples e a um campo magnético externo uniforme. Nossa análise emprega um domínio numérico tridimensional onde gotas monodispersas de ferrofluido estão suspensas aleatoriamente em um fluido carreador Newtoniano não magnético. As equações de Navier-Stokes incompressíveis são resolvidas usando um método de projeção de segunda ordem. Além disso, utilizamos o método de level set para capturar a interface e, assumindo que as superfícies das gotas estão livres de surfactantes, implementamos uma força repulsiva entre elas para evitar a coalescência. Definimos diferentes concentrações de gotas, números de capilaridade e números de capilaridade magnética. Primeiro, na ausência de campo magnético, determinamos a viscosidade efetiva variando as concentrações de gotas e os fluxos de cisalhamento, obtendo resultados que concordam bem com trabalhos anteriores. Posteriormente, observamos que a deformação e o ângulo de inclinação das gotículas aumentam com o número capilar magnético, enquanto diminuem quando a fração de volume aumenta. O ângulo de inclinação é o ângulo entre o eixo principal da gotícula e a direção principal do fluxo (direção x). Constatamos que as interações entre gotas podem alterar significativamente a dinâmica e a geometria das gotas, levando a uma resposta dinâmica. Essas mudanças geométricas causam variações tanto na viscosidade quanto na magnetização média da emulsão. À medida que o número de capilaridade magnética e a fração volumétrica aumentam, ambas as propriedades se elevam. No entanto, quando normalizadas pela fração volumétrica, observamos que as gotas em regimes diluídos contribuem mais significativamente para essas propriedades médias. Apesar da hipótese superparamagnética, calculamos um ângulo de desalinhamento entre a magnetização e o campo magnético externo, gerando torques nas gotas. Para baixos números de capilaridade, um aumento na concentração de gotas reduz o ângulo, enquanto para concentrações mais altas, o ângulo aumenta. No geral, investigamos os efeitos que a presença de múltiplas gotas de ferrofluido causa nas propriedades médias da emulsão.

Palavras-chaves: emulsão magnética, emulsão concentrada, cisalhamento simples, método de level set

Dedico esta dissertação ao meu avô. Mais que sua neta, sou sua fã.

Acknowledgements

Esta dissertação não teria sido concluída sem o apoio e orientação de algumas pessoas e instituições. Por isso, agradeço imensamente cada um citado. Ao professor Taygoara Oliveira pelo essencial apoio durante todo o mestrado, pela orientação e oportunidade de estudar este tema. Obrigada por sempre receber todos os alunos com atenção. Sem o seu apoio eu definitivamente não teria concluido o mestrado, mil obrigadas. Agradeço também aos professores Aline de Paula e Adriano Fabro por disponibilizarem gentilmente alguns dos computadores usados para as simulações desta dissertação. De modo geral, a todos os professores do ENM que contribuíram para a minha formação. Agradeço ao Lucas Hildebrand por me coorientar e pelas inúmeras ajudas que foram fundamentais para a conclusão deste trabalho, além das reuniões nas quais aprendi bastante. Agradeço também ao professor Francisco Ricardo pelas excelentes aulas das quais tive a oportunidade de participar.

A todos os colegas do grupo de gotas. Porém, especialmente àqueles que me ajudaram diretamente neste trabalho: Arthur, Lucas, Juan e Victor. Obrigada por sempre estarem dispostos a ajudar. Arthur e Juan obrigada pela ajuda de cada dia e pelas várias discussões enriquecedoras; o mestrado se tornou uma experiência mais memorável com a companhia de vocês. Agradeço também a todos os demais alunos do LEA e do GDS pelos momentos de descontração.

Apesar de desafiador, ingressar e concluir a pós-graduação também é um privilégio, especialmente num país desigual como o Brasil. Agradeço à FAP-DF, à CAPES e ao CNPq pelo suporte financeiro durante a realização desta dissertação. À Universidade de Brasília e todas as instituições públicas que frequentei durante grande parte da minha vida.

E termino com o mais importante: minha família. Agradeço à Cida; mãe, obrigada por cuidar da minha dog Ravena quando eu estive longe, sem o seu apoio muitos sonhos, olhares e caminhos não seriam possíveis. À minha irmã, Rayane, por sempre estar ao meu lado e me inspirar. Aos meus amados avós, à dindinha, aos primos, tias, tios; à tia Lourdes, com imensa saudade. Agradeço pelo carinho e por sentir tanto amor por vocês.

Contents

List of Figures

List of Tables

1 Introduction

1.1 What are ferrofluid emulsions and why are they important?

Ferrofluid emulsions are a subset of magnetic emulsions found within the larger group of microstructured soft materials. Lately, this system has gained attention due to its potential for remote control and has become the basis for many high-tech devices in the field of microfluidics (Sun et al., 2023). Such a dispersion is created by mixing an oil-based ferrofluid with another non-magnetic immiscible fluid. In this context, either the dispersed fluid or the carrier fluid can be the ferrofluid phase. However, in this work, only emulsions made of ferrofluid droplets are considered.

Emulsions are unstable dispersions in which droplets are subjected to various types of forces and may tend to come closer to each other, leading to destabilization processes such as coalescence (i.e. the formation of larger droplets). Thus, the addition of a surfactant is necessary to maintain the stability of the system for a long time, achieving a metastable state. Meanwhile, ferrofluids are also unstable mixtures, but instead of liquid droplets, they consist of rigid magnetic nanoparticles suspended in a Newtonian liquid. These nanoparticles must be coated with surfactants to prevent aggregation and maintain stability. When there is no external magnetic field, particles are randomly oriented and do not exhibit magnetic behavior. However, when a magnetic field is applied, the magnetic dipole moments of each particle align with the direction of the external field. On average, this leads the material to exhibit magnetic properties. The first reported preparation process of a monodisperse ferrofluid emulsion was by Bibette (1993). In their experiment, the sodium dodecyl sulfate (SDS) surfactant was dissolved in distilled water, forming the continuous phase. Then, the dispersed phase composed of kerosene ferrofluid was slowly added to the first solution under a small shear, resulting in the ferrofluid emulsion. Since this system is highly polydisperse, a purification method is applied to transform it into a monodispersed emulsion, with droplet diameters of about 0.7 micrometers. Later, Montagne et al. (2002) obtained droplets with a narrow size distribution using only a magnetic field (see Figure 1.1 (a)).

Although typical emulsions have fascinating dynamics that depend on their microscopic droplet structure, imposed flow, and composition that modify the macroscopic proprieties, ferrofluid emulsions can be even more interesting. For example, the generation and manipulation of droplets in microchannels are a subcategory of microfluidics that has emerged as a versatile tool for biological and chemical applications (Teh et al., 2008). In this context, more precise control of generating droplets with specific sizes is achieved by using a ferrofluid emulsion and applying a magnetic field at a microfluidic T-junction (Tan and Nguyen, 2011, Tan et al., 2010). Also, liquid microrobots based on ferrofluid droplets, as shown in Figure1.1 (b), have been developed to enable access to hard-to-reach regions within the human body for less invasive medical procedures, by altering their shape through the use of different magnetic field strengths (Fan et al., 2022, 2020).

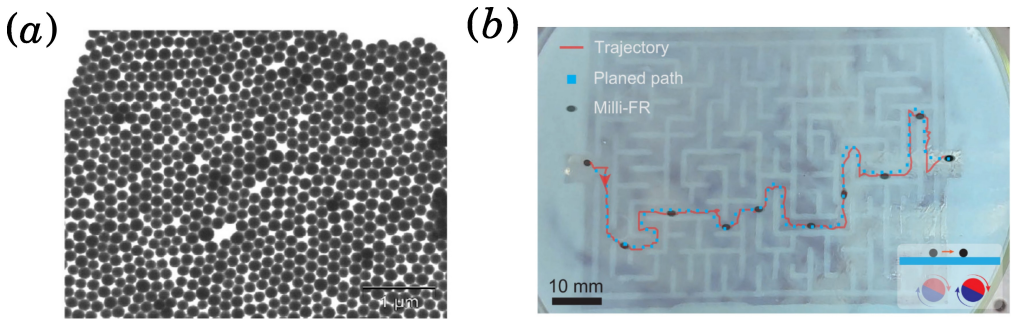

Figure 1.1 – (a) Monodisperse magnetic emulsion observed under a transmission electron microscope. Taken from Montagne et al. (2002). (b) Millimeter-scale ferrofluidic robots induced by magnetic drag force to navigate through a complex geometry. Taken from Fan et al. (2022).

At a fundamental level, these applications rely on the fact that ferrofluid droplets, when subjected to an external magnetic field, introduce an additional relaxation mechanism to the dynamics of the emulsion. Now, not only the external flow distorts their equilibrium microstructure, but also a magnetic field. There is a competition where the interfacial tension tends to maintain the droplet in a spherical shape while the external magnetic field induces stretching. As an example, in Figure 1.2 (a), one can see a single ferrofluid droplet in a viscous medium subjected to a pure external magnetic field. Note that as the strength of this field increases, the droplets are gradually stretched and oriented in the same direction. Inside the droplet, what happens is that the suspended magnetic nanoparticles experience dipolar interactions, leading to the formation of chains and migration toward the contact line of the droplet

(Shyam et al., 2020). This also means that the average alignment of the dipole moments of the magnetic particles increases. This value per unit of volume is known as the magnetization vector **M**. When the external magnetic field is strong enough and this quantity does not vary at all, we call it saturation magnetization, and the droplet no longer changes its shape at this limit.

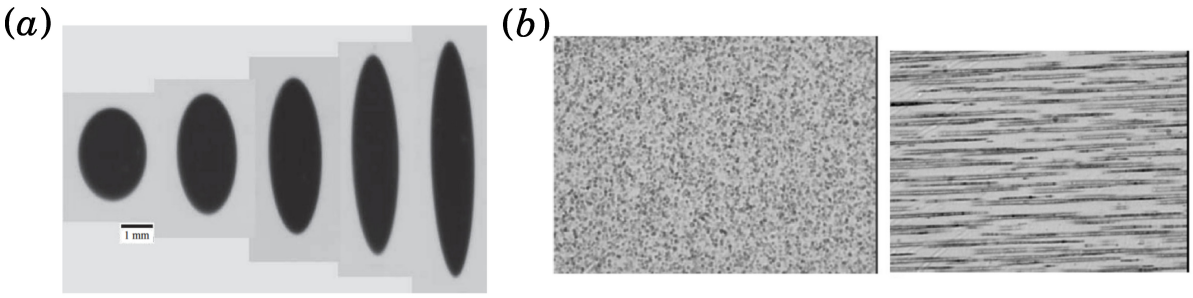

Figure 1.2 – (a) The deformation of the ferrofluid droplet shape intensifies with the increase of the external magnetic field; adapted from Afkhami et al. (2010). (b) Magnetic emulsion in the absence of external magnetic field and the presence, respectively; taken from Montagne et al. (2002).

In emulsion rheology, the volume fraction of the dispersed phase Φ, determines if the emulsion is dilute, semi dilute or concentrated. Depending on these values the relationship between stress and strain rate will significantly change. At low volume fraction (i.e. dilute regime, see Figure 1.3) and small deformation limit, where there is no hydrodynamics interactions or other types of interactions between the drops, the emulsion behaves as a Newtonian fluid (purely viscous). It also means that the viscosity has a linear dependence with Φ. However, as the volume fraction of the droplets increases, droplet-droplet interactions become significant. Therefore, higher orders of the volume fraction must be taken into account to determine the bulk viscosity in a theoretical asymptotic analysis. Moreover, at low interfacial tension, non-Newtonian effects begin to appear regardless of the volume fraction value. Let us consider a simple shear case: as the shear rate increases, the droplets tend to align in the direction of the flow, and this alignment enhances shear-thinning behavior, in which viscosity decreases with increasing shear rate. Thus, the complex dynamics arises from the fact that the droplets are deformable particles. On the other hand, when we add a large quantity of droplets until we cannot add one more without deforming the others, we achieve the randomly close-packed state, which is approximately $\Phi_{RCP} \approx 0.64$. At this value the droplets are separated by very thin

liquid films, leading to elastic behavior (Otsubo and Prud'homme, 1994). When the randomly close-packed value is exceeded, the emulsion becomes jammed and may exhibit a transition point known as yield stress. Below this point, the emulsion undergoes reversible elastic deformation, similar to a solid. Above this point, it exhibits irreversible viscoplastic flow. Thixotropy is another typical response of emulsions. Different from viscoelasticity, the thixotropy has a reversible, inelastic, time dependence of the viscosity or yield stress (Larson and Wei, 2019). This is associated with time-dependent droplet aggregation or rearrangements.

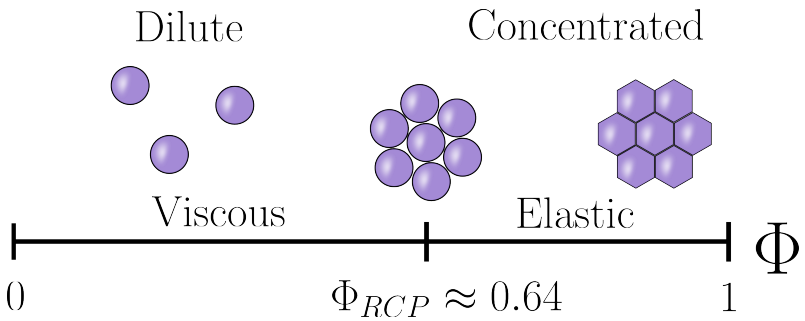

Figure 1.3 – Schematic representation of how monodispersion emulsions behave as a function of volume fraction, also indicating the value of the randomly close packed (RCP) and the microstructure arrangement of the drops. Image inspired by Mason (1999).

The combination of concentrated ferrofluid emulsions and the analysis of the bulk properties of these materials while examining their microstructural state has not been discussed thoroughly. In recent years, a large number of numerical and experimental studies have aimed to determine both the magnetic and rheological properties of single ferrofluid droplets (Abicalil et al., 2021, Afkhami et al., 2010, Cunha et al., 2020, Guilherme et al., 2023). These studies have provided invaluable insights into how these materials respond to imposed flows and no-flow conditions in the presence of an applied external magnetic field. However, contrary to the analysis of single ferrofluid droplets, when we introduce more droplets into the system, they not only deform in response to the external field but also interact with each other. Figure 1.2 (*b*) shows, from a transmission electron microscope, a concentrated magnetic emulsion. In the left figure, where there is no external magnetic field applied, the droplets are randomly distributed and behave similarly to a typical emulsion. In the right, under an applied magnetic field, the ferrofluid droplets tend to align in the same direction of the applied field while deforming to a nonspherical shape, experiencing a

complex self-organization process that may form chains. In this context, this dissertation focuses on measuring bulk magnetic properties and analyzing the microscopic structure of these emulsion, elucidating the influence of the volume fraction, interfacial tension, and magnetic field on this system.

1.2 Literature review

Considering our interest in the response of concentrated ferrofluid emulsions under an external magnetic field, it is relevant to highlight contributions from articles on non-colloidal suspensions of rigid particles and droplet dispersions, both in dilute and concentrated regimes, whether magnetic or not. These contributions provide insights into our study system and support this work.

The dynamics and rheological response of non-Brownian hard spheres suspended in a carrier Newtonian fluid have been under investigation for over a century. At very low particle concentrations, Einstein (1906, 1911) was the first to theoretically quantify the linear increase in effective viscosity as a function of volume fraction. Later, attempts were made to extend the theory to higher concentrations, revealing that viscosity increased more rapidly than predicted by the linear expression $\eta_{eff} = \eta_c(1 + c\Phi)$. Here, η_c represents the viscosity of the carrier fluid and c is a constant, which in Einstein's theory is equal to 5/2. Batchelor (1972) was the first to determine viscosity considering a second-order correction in the volume fraction $\mathcal{O}(\Phi^2)$, i.e., considering pairwise interactions. For higher particle concentrations, numerical and experimental works play an important role in predicting the behavior of suspensions. Brady and Bossis (1985) and Sierou and Brady (2002) point out that the increase in viscosity with increasing particle concentration is due to the formation of particle clusters. They also note that the anisotropic structure resulting from interparticle forces leads to normal stress differences, which consequently contributes to the non-Newtonian behavior of the suspensions.

When we consider droplets instead of rigid particles, the behavior of the materials can be entirely different. Even in low dispersed concentrations, Taylor (1932) showed under the assumption of low shear rates (droplets remain nearly spherical) that effective viscosity is $\eta_{eff} = \eta_c(1 + 5/2\Phi(\lambda + 2/5)/(\lambda + 1))$. In the limit of a viscosity

ratio $\lambda \to \infty$, the Einstein expression for hard spheres is recovered. In contrast, when $\lambda \to 0$ the expression simplifies to $\eta_{eff} = \eta_0(1+\Phi)$, characterizing the foam regime. Most of the reported research on single droplet emulsions focuses on determining the deformation, orientation, particle stress tensor, and breakup regime under an imposed flow. Besides the pioneering work of Taylor (1934), in which a deformation model was formulated at the limit of spherical drop shape, several numerical and experimental studies have been developed. Under shear flow, using different methods, Kennedy et al. (1994), Kwak and Pozrikidis (1998) and Guido and Villone (1998) investigated the deformation and orientation of drops for a wide range of viscosity ratios and flow strengths. Also some works considered the effect of confinement (Guido, 2011, Ioannou et al., 2016). A good review on this topic was made by Rallison (1984). As the flow rate increases, the droplets become more deformed, assume a prolate ellipsoid shape and continue to deform until they breakup. Amani et al. (2019) investigated the critical conditions that lead to droplet breakup using level set method. Another important contribution to dilute suspensions of deformable particles was the calculation of the stress of each particle relative to the bulk stress using the particle stress tensor developed by Batchelor (1970).

For higher droplet concentrations, studies focus on investigating the macroscopic dynamics of the emulsion due to the complexity of computing the interactions between the droplets, which makes the problem more nonlinear. Thus, most papers are experimental and numerical. Loewenberg and Hinch (1996) were the first to measure the rheological properties of emulsions with volume fractions up to 30% in simple shear flow using the boundary integral method (BIM). Later, under a similar numerical methodology, Loewenberg (1998) simulated pressure-driven flows and also made predictions about the emulsion microstructure. Zinchenko and Davis (2002) developed an efficient algorithm for hydrodynamic interactions using BIM, achieving higher droplet volume fractions. Srivastava et al. (2016) studied the effective rheology in the presence of finite inertia using the front-tracking method at moderate regime concentrations. Meanwhile, several experimental studies have determined the shear viscosity as a function of the particle volume fraction (Faroughi and Huber, 2015, Pal, 2001). Jansen et al. (2001) experimentally studied the conditions for droplet breakup under simple shear for concentrated emulsions. Moreover, coalescence is another important process investigated by Shardt et al. (2013) and Yang et al. (2001) through the approach of two equal-size droplets in simple shear. In

recent years, there have been studies on multiphase flows with multibody interactions using interface capturing methods. Rosti et al. (2019) used the volume of fluid method to study the rheology of the system, while De Vita et al. (2019) similarly investigated the coalescence process and rheology using a repulsive force. At high volume fractions, when droplets lose their spherical shape and become polygonal, interesting effects emerge, such as a plastic-like response to shear deformations and the presence of yield stress and interface layers, as evidenced by Mason et al. (1996), Derkach (2010), and Kondaraju et al. (2012).

Since the synthesis of ferrofluid emulsions reported by Bibette (1993), there has been a growing interest in studying this type of system. In the diluted regime, the effect of applied magnetic fields on the shape of ferrofluid droplets and orientation angle in a simple shear flow has been widely investigated (Afkhami et al., 2010, Capobianchi et al., 2018, Cunha et al., 2018, Hassan et al., 2018, Jesus et al., 2018). They reported that, at a fixed shear flow, an increase in the magnetic field strength increases the deformation of the droplet and tends to align it along the external field. Also, the conditions for droplet breakup were investigated by Cunha et al. (2018) and Kawabata et al. (2024) in shear flows. Their study revealed that the external magnetic field can either inhibit or promote droplet breakup, depending on its direction and strength. Changes in microstructure significantly influence the macroscopic behavior of the emulsion. Thus the bulk shear viscosity and differences in normal stresses in the presence of an external magnetic field were determined by Capobianchi et al. (2021), Abicalil (2021), Ishida and Matsunaga (2020), Cunha et al. (2020). Moreover, Abicalil et al. (2021) measured the bulk magnetization under shear and also quantified a misalignment between the bulk magnetization and the external magnetic field, which generates a magnetic torque acting on the droplet. Abdo et al. (2023) determined this under small amplitude oscillatory shear flows. In contrast to diluted ferrofluid emulsions, studies on systems considering droplet-droplet interactions are scarce. While Wu and Yao (1999) observed structure formation under an applied magnetic field using an optical microscope, Hassan and Wang (2020) focused on pairwise interactions between ferrofluid droplets. As far as we know, no studies have examined both the rheological and magnetic properties of ferrofluid emulsions at moderate concentrations.

1.3 Problem setup

In this work, we investigated the behavior of ferrofluid droplets immersed in a non-magnetic Newtonian fluid at moderate concentrations. The volume fraction of the droplets ranges from $\Phi = 0.10$ to $\Phi = 0.30$. Figure 1.4 shows a snapshot from the simulations at $\Phi = 0.20$. The numerical domain is three-dimensional (3D), with walls of equal length L. At time zero, all droplets are spherical with a unity radius r and are randomly distributed. The system is subjected to both a simple shear flow with a shear rate $\dot{\gamma}$ and an external uniform magnetic field $\mathbf{H}_0$ applied only in the y direction. The domain is periodic in the x and z directions, while the walls in y direction have a no-slip and impenetrable boundary condition. These walls move with a speed of $\dot{\gamma}L/2$ in opposite directions. We consider neutrally buoyant drops with a viscosity ratio of unity. A low Reynolds number is assumed, $Re = 0.01$. Moreover, we use a level set method to capture the interface and a projection method to solve the flow field. These numerical methods have been implemented in an in-house Fortran code called FENRir (Ferrofluid Emulsion Numerical Rheometer).

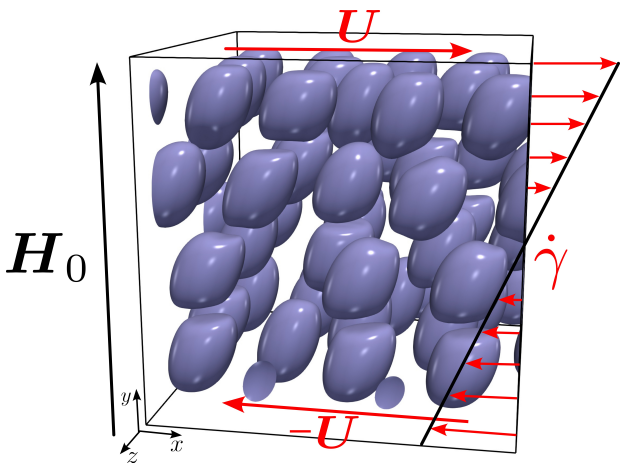

Figure 1.4 – Schematic illustration of the problem in this study. The droplets are immersed in a cubic domain and subjected to a simple shear flow with a shear rate $\dot{\gamma}$. The top wall has a velocity $U = \dot{\gamma}L/2$, and the bottom wall has the same magnitude but in the opposite direction, where L represents the distance between the walls. Also an external uniform magnetic field is applied $\boldsymbol{H}_0$.

2 Theoretical fundamentals

This chapter provides an overview of the mathematical formulation and theoretical concepts necessary for understanding the behavior of magnetic droplets, which combines fluid dynamics and electromagnetic theory. First, the balance equations for fluid flow with a moving interface based on the continuum approach are shown. Then, Maxwell's equations will be presented in the context of ferrofluids, including the magnetic body force and the main emulsion properties used throughout this work. Finally, the dimensionless equation and the main dimensionless numbers are presented.

2.1 Balance equations for two-phase flows

This work focuses on droplet dynamics, and we employ the single fluid formulation for two-phase flows. In this context, fluid motion is governed by the following equations derived from balance laws

$$\nabla \cdot \mathbf{u} = 0, \tag{2.1}$$

$$\rho(\mathbf{x})\left(\frac{\partial \mathbf{u}}{\partial t} + \mathbf{u} \cdot \nabla \mathbf{u}\right) = \nabla \cdot \boldsymbol{\Sigma} + \mathbf{f}_{\text{cap}}\delta(\mathbf{x} - \mathbf{x}_\Gamma) + \mathbf{f}_{\text{mag}}, \tag{2.2}$$

where the first equation is related to the mass conservation principle for an incompressible flow, while the second one is the Cauchy equation with an added term of body force due to interfacial tension $\mathbf{f}_{\text{cap}}$ and a magnetic force $\mathbf{f}_{\text{mag}}$. Here, ρ represents the density, which is a position-dependent variable, $\mathbf{u}$ is the velocity field, δ is the Dirac delta function, $\mathbf{x}_\Gamma$ is a point on the interface, and $\boldsymbol{\Sigma}$ is the stress tensor. Buoyancy effects are considered negligible, and the densities of the phases are assumed to be equal. For an Newtonian fluid, the stress tensor is defined as

$$\boldsymbol{\Sigma} = -p\mathbf{I} + 2\eta(\mathbf{x})\mathbf{D}, \tag{2.3}$$

where p is the pressure and $\mathbf{I}$ is the identity tensor. These quantities together define the isotropic part of the stress tensor. The second term on the right-hand side is the deviatoric part, where $\mathbf{D} = 1/2\left[\nabla\mathbf{u} + (\nabla\mathbf{u})^{\mathrm{T}}\right]$ is the strain rate tensor and η the viscos-

ity, which is considered equal for both phases. In two-phase flows, there is a stress jump at the interface between the fluids. Hence we can determine the capillary force, which is a force per unit area acting perpendicularly at each point of the interface, by balancing the hydrodynamic traction exerted by the fluid on both sides of the interface. However, as pointed out by Tryggvason et al. (2011), we can also define a constitutive equation for the interface by defining an isotropic surface stress tensor as

$$\boldsymbol{\Sigma}_S = \sigma \mathbf{I}_S, \tag{2.4}$$

where $\mathbf{I}_S = (\mathbf{I} - \hat{\mathbf{n}}\hat{\mathbf{n}})$ is the surface identity tensor, $\hat{\mathbf{n}}$ denotes the outward unit vector normal to the interface, and σ is the interfacial tension coefficient or just interfacial tension. The capillary body force (force per volume) is equivalent to the divergence of the surface stress tensor

$$\mathbf{f}_{cap} = -\nabla_S \cdot \boldsymbol{\Sigma}_S, \tag{2.5}$$

where $\nabla_S = \mathbf{I}_S \cdot \nabla$ is the surface gradient operator. Using vector identities, we can rewrite equation (2.5) as

$$\mathbf{f}_{cap} = \sigma(\nabla_S \cdot \hat{\mathbf{n}})\hat{\mathbf{n}} - \nabla_S \sigma. \tag{2.6}$$

The first term on the right hand side is associated with a normal stress jump or capillary pressure, which is equivalent to the Young-Laplace equation. We define the local mean curvature of the interface throughout the computational domain,

$$\kappa = -\nabla_S \cdot \hat{\mathbf{n}}. \tag{2.7}$$

The second term on the right-hand side of equation (2.6) is associated with a tangential stress jump, related to the presence of an interfacial tension gradient known as Marangoni effects. This work solely considers the normal stress component, assuming $\nabla_S \sigma = 0$; in other words, we consider a clean interface (no surfactants). For a control volume within the entire domain Ω that includes the interface Γ, the capillary force is calculated by integration along Γ. To include this force in equation (2.2), we need to convert it from a surface integral over the interface to a volume integral. Since the capillary force is zero everywhere except at the interface, we can use the Dirac delta function (three-dimensional version), thus we have that

$$\int_\Gamma \mathbf{f}_{cap} dS = \int_\Omega \mathbf{f}_{cap} \delta(\mathbf{x} - \mathbf{x}_\Gamma) dV. \tag{2.8}$$

Applying the localization theorem (Aris, 2012), we get that

$$\mathbf{f}_{\text{cap}}\delta(\mathbf{x}-\mathbf{x}_\Gamma) = -\sigma\kappa\delta(\mathbf{x}-\mathbf{x}_\Gamma)\hat{\mathbf{n}}, \tag{2.9}$$

which is the capillary force added to the Navier-Stokes equations to obtain a single-fluid formulation for flows with interfaces.

2.2 Ferrohydrodynamics concepts

Ferrofluids, also known as magnetic fluids, are stable suspensions of magnetic nanoparticles (approximately 10 nm in diameter) in a Newtonian liquid. These fluids are classified as superparamagnetic. To understand ferrohydrodynamics (FHD), we begin with Maxwell's equations, which describe most problems involving electric and magnetic phenomena. In their differential forms, Maxwell's equations are given by

$$\begin{aligned}
&\nabla\cdot\mathbf{E} = \frac{\rho_e}{\epsilon_0}, && \text{(Gauss' law of electricity)}\\
&\nabla\cdot\mathbf{B} = 0, && \text{(Gauss' law of magnetism)}\\
&\nabla\times\mathbf{E} = -\frac{\partial\mathbf{B}}{\partial t}, \quad \text{and} && \text{(Faraday's law)}\\
&\nabla\times\mathbf{B} = \mu_0\mathbf{J} + \mu_0\epsilon_0\frac{\partial\mathbf{E}}{\partial t}. && \text{(Ampère-Maxwell's law)}
\end{aligned} \tag{2.10}$$

Here, $\mathbf{E}$ represents the electric field, $\mathbf{B}$ is the magnetic induction field, ρ_e is the electric charge density, ϵ_0 is the permittivity of free space, μ_0 is the magnetic permeability of free space, and $\mathbf{J}$ is the total electric current density. For magnetized (or polarized) matter, it is given by $\mathbf{J} = \mathbf{J}_f + \mathbf{J}_p$, where $\mathbf{J}_f$ is the free-charge current density and $\mathbf{J}_b$ is the bound current density, which is related to the magnetization vector $\mathbf{M}$ by (Griffiths, 2023)

$$\mathbf{J}_b = \nabla\times\mathbf{M}. \tag{2.11}$$

In FHD, the magnetostatic regime is considered, characterized by the absence of both free electric charge ($\mathbf{J}_f = 0$, non-conducting fluid) and the electric field ($\mathbf{E} = 0$). Substituting equation (2.11) into the Ampère–Maxwell's law yields:

$$\nabla\times\mathbf{B} = +\mu_0\nabla\times\mathbf{M} \tag{2.12}$$

$$\nabla \times \mathbf{B} - \mu_0 \nabla \times \mathbf{M} = 0 \tag{2.13}$$

$$\nabla \times \left(\frac{1}{\mu_0} \mathbf{B} - \mathbf{M} \right) = 0. \tag{2.14}$$

The quantity in parentheses, denoted by $\mathbf{H}$, represents the magnetic field. Combining this concept, Maxwell's equations for the magnetostatic regime can be summarized as follows:

$$\nabla \cdot \mathbf{B} = 0 \tag{2.15}$$

$$\nabla \times \mathbf{H} = 0 \tag{2.16}$$

where $\mathbf{B}$ can be written as

$$\mathbf{B} = \mu_0 (\mathbf{M} + \mathbf{H}), \tag{2.17}$$

which is composed of a contribution from the magnetic field and the material magnetization. In this work, the magnetization vector is always locally parallel to the magnetic field (in the limit of small $\mathbf{H}$). This allows us to define the following superparamagnetic relationship:

$$\mathbf{M} = \chi \mathbf{H}, \tag{2.18}$$

where $\chi(\mathbf{x}) = (\mu(\mathbf{x})/\mu_0 - 1)$ represents the magnetic susceptibility. Note that the magnetic permeability of the continuous phase is equal to the magnetic permeability of free space, since this fluid is non-magnetic, which leads to $\chi = 0$. To generalize this quantity to the entire domain, we define the permeability ratio $\zeta(\mathbf{x}) = \mu(\mathbf{x})/\mu_0$. Thus, $\zeta = 1$ outside the ferrofluid droplets, and $\zeta(\mathbf{x}) = 1 + \chi$ inside the droplets. Substituting this into equation (2.17), we have

$$\mathbf{B} = \mu_0 \zeta(\mathbf{x}) \mathbf{H}. \tag{2.19}$$

If $\mathbf{J}_f = 0$ everywhere, the curl of $\mathbf{H}$ vanishes (equation (2.16)), and we can express $\mathbf{H}$ as the gradient of a scalar potential ψ:

$$\mathbf{H} = -\nabla \psi. \tag{2.20}$$

Combining equation (2.15) with equations (2.19) and (2.20) gives

$$\nabla \cdot \left(\mu_0 \zeta(\mathbf{x}) \nabla \psi \right) = 0. \tag{2.21}$$

The boundary conditions for the magnetic potential equation above are described in Section 2.2.1. The applied external magnetic field results in a force, known as the Kelvin force, acting on a magnetic droplet (Rosensweig, 2013):

$$\mathbf{f}_{\text{mag}} = \mu_0 \mathbf{M} \cdot \nabla \mathbf{H}, \tag{2.22}$$

where $\mathbf{M}$ is the bulk magnetization of a droplet resulting from the mean of all magnetic dipole vectors inside it, given by

$$\mathbf{M} = \frac{1}{V_d} \sum_{i=1}^{N} \mathbf{m}_i \tag{2.23}$$

where V_d is the volume of the dispersed phase and $\mathbf{m}$ is the magnetic dipole moment of a magnetic droplet. In this work, we compute the bulk magnetization of the emulsion,

$$\langle \mathbf{M} \rangle = \frac{1}{Vc} \int_{\Omega} \left(\zeta(\mathbf{x}) - 1 \right) \mathbf{H} dV_c \tag{2.24}$$

where V_c is the the volume of the system, which encompasses the entire computational domain Ω, so we take the average magnetization over the entire computational domain. Using the linear relationship between the magnetization vector and the magnetic field, the magnetic force can be written as

$$\mathbf{f}_{\text{mag}} = \mu_0 (\zeta(\mathbf{x}) - 1) \mathbf{H} \cdot \nabla \mathbf{H}. \tag{2.25}$$

Note that ζ is not a constant parameter over the entire space, at the interface there is a jump in this value and also a gradient in $\mathbf{H}$, which induce magnetic forces at the interface. Thus, in the presence of magnetic fields, the magnetic droplet surface experiences a capillary and magnetic stress jumps Guilherme et al. (2023),

$$\hat{\mathbf{n}} \cdot [\![\Sigma_T]\!] = -\sigma \kappa \hat{\mathbf{n}} + \frac{1}{2} \mu_0 \left(\zeta(\mathbf{x}) - 1 \right) ||\mathbf{H}||^2 \hat{\mathbf{n}} \tag{2.26}$$

where $[\![\cdot]\!]$ represents the jump of a quantity across the interface between the two fluids, Σ_T represents the total stress contributions from the Newtonian and ferrofluid phases, and $||\mathbf{H}||$ is the magnitude of the magnetic field.

2.2.1 Boundary conditions for magnetic potential

To ensure the continuity of the magnetic field when the droplet crosses the domain, we impose a periodic condition in the xz-direction for the magnetic field. To achieve this, we redefine the magnetic field as

$$\mathbf{H} = \mathbf{H}_0 + \mathbf{H}_\mathrm{P} \tag{2.27}$$

where $\mathbf{H}_\mathrm{P}$ is the periodic magnetic field and $\mathbf{H}_0$ is the uniform magnetic field. Substituting the equation (2.27) into equation (2.16), we obtain:

$$\nabla \times (\mathbf{H}_0 + \mathbf{H}_\mathrm{P}) = 0. \tag{2.28}$$

Since the uniform magnetic field is, by definition, a curl-free field, it follows that the curl of $\mathbf{H}_\mathrm{P}$ also vanishes. In this context, the magnetic induction field becomes

$$\mathbf{B} = \mu_0 \zeta(\mathbf{x})(\mathbf{H}_0 + \mathbf{H}_\mathrm{P}). \tag{2.29}$$

In this case, it is possible to define a magnetic potential for both magnetic fields: $\mathbf{H}_0 = -\nabla\psi_0$ and $\mathbf{H}_\mathrm{P} = -\nabla\psi_\mathrm{P}$. Applying this to equation (2.29) and taking the divergence, we have that

$$\nabla \cdot \big(\zeta(\mathbf{x})\nabla\psi_0\big) + \nabla \cdot \big(\zeta(\mathbf{x})\nabla\psi_\mathrm{P}\big) = 0. \tag{2.30}$$

Given that $\nabla\psi_0 = -\mathbf{H}_0$ and $\mathbf{H}_0$ is uniform, we obtain $\nabla \cdot (\nabla\psi_0) = 0$. Then,

$$\nabla \cdot \big(\zeta(\mathbf{x})\nabla\psi_\mathrm{P}\big) = \nabla\zeta(\mathbf{x}) \cdot \mathbf{H}_0 \tag{2.31}$$

Therefore, periodic boundary conditions are applied in the x and z directions through equation (2.31), while for the y-direction we apply the Neumann condition $\hat{\mathbf{n}} \cdot \nabla\psi_\mathrm{P} = 0$.

2.3 The viscosity of emulsions

A classic approach to studying the rheology of emulsions involves subjecting the emulsion system containing droplets confined between two parallel walls to simple shear flow. To describe the overall dynamics of the emulsion, we compute macro-

scopic properties. It should be pointed out, however, that because of the presence of repulsive forces between the droplets, we cannot determine the contribution of each individual droplet to the bulk stress of the emulsion in this work. In other words, we cannot calculate the stresslet. Therefore, we determine the effective shear viscosity of the ferrofluid emulsion as:

$$\eta_{eff} = \frac{\langle \Sigma_{yx} \rangle}{\dot{\gamma}} \tag{2.32}$$

where

$$\langle \Sigma_{yx} \rangle = \frac{1}{2L_x L_z} \int_A \eta_c \frac{\partial u}{\partial y} dA \tag{2.33}$$

is the average shear stress on the plates. Here, we are integrating the stress that the fluid exerts on the plate over its entire area A, and dividing by the total area of the two plates $2L_xL_z$. The reduced viscosity, which is the effective viscosity minus the base fluid viscosity, is also determined in this work as

$$\eta_{red} = \frac{\langle \Sigma_{yx} \rangle - \eta_c \dot{\gamma}}{\eta_c \dot{\gamma}}. \tag{2.34}$$

A great effort has been made to describe the effect of volume fraction on the effective viscosity of emulsions. Pal (2001) formulated a model that describes the experimental viscosity data very well,

$$\eta_r \left[\frac{2\eta_r + 5\lambda}{2 + 5\lambda} \right]^{3/2} = \left(1 - \frac{\Phi}{\Phi_m} \right)^{-2.5\Phi_m}. \tag{2.35}$$

where $\eta_r = \eta_{eff}/\eta_c$ is the relative viscosity, $\phi_m = 0.637$ corresponds to the random close packing of hard spheres, and λ is the viscosity ratio between the two phases. We compare our simulation with this model in Section 4.2.

2.4 Dimensionless governing equation

Expressing the main governing equations in dimensionless terms is more appropriate because it allows for easier interpretation of crucial parameters that govern the flow behavior under analysis. For this purpose, characteristic parameters and

dimensionless variables are introduced, which in this study are

$$\mathbf{u}^* = \frac{\mathbf{u}}{\dot{\gamma} r}, \quad t^* = t\dot{\gamma}, \quad \mathbf{x}^* = \frac{\mathbf{x}}{r}, \quad p^* = \frac{p}{\rho r^2 \dot{\gamma}^2}, \quad \kappa^* = r\kappa, \quad \nabla^* = r\nabla$$
$$\delta^* = r\delta, \quad \rho^* = \frac{\rho(\mathbf{x})}{\rho_c}, \quad \lambda = \frac{\eta(\mathbf{x})}{\eta_c}, \quad \mathbf{H}^* = \frac{\mathbf{H}}{H_0}, \quad \text{and} \quad \psi* = \frac{\psi}{rH_0},$$

where r is the droplet radius and subscript c is related to properties of the continuous phase. In this work, the system is in neutral buoyancy with a unit viscosity ratio. Substituting these non-dimensional parameters into equations (2.1), (2.2), and (2.31) and dropping the superscript $*$, we get

$$\nabla \cdot \mathbf{u} = 0, \tag{2.36}$$

$$\frac{\partial \mathbf{u}}{\partial t} + \mathbf{u} \cdot \nabla \cdot \mathbf{u} = -\nabla p + \frac{1}{\mathrm{Re}} \nabla \cdot [2\mathbf{D}] - \frac{1}{\mathrm{Re}\,\mathrm{Ca}} \kappa \delta(\mathbf{x} - \mathbf{x}_\Gamma)\hat{\mathbf{n}} + \frac{\mathrm{Ca}_{\mathrm{mag}}}{\mathrm{Re}\,\mathrm{Ca}} (\zeta(\mathbf{x}) - 1)\mathbf{H} \cdot \nabla \mathbf{H}, \tag{2.37}$$

and

$$\nabla \left(\zeta(\mathbf{x}) \nabla \psi \right) = -\nabla \zeta(\mathbf{x}) \cdot \mathbf{H}_0. \tag{2.38}$$

where

$$\mathrm{Re} = \frac{\rho \dot{\gamma} r^2}{\mu_c} \tag{2.39}$$

is the Reynolds number, which represents the ratio of inertial to viscous effects, and

$$\mathrm{Ca} = \frac{\eta_c \dot{\gamma} r}{\sigma} \tag{2.40}$$

is the capillary number. When subjected to simple shear, Ca represents the relative importance between viscous and interfacial tension effects, and can also be interpreted as a ratio between a droplet relaxation time due to interfacial tension and a characteristic flow time. Moreover,

$$\mathrm{Ca}_{\mathrm{mag}} = \frac{\mu_0 r H_0^2}{\sigma} \tag{2.41}$$

is the magnetic capillary number, which represents the relative importance between viscous effects and the magnetic effect on the droplet shape. Another important dimensionless parameter is the volume fraction of droplets

$$\Phi = \frac{N V_d}{V_c}, \tag{2.42}$$

where N is the number of droplets, $V_d = 4/3\pi r^2$ is the volume of a droplet, and $V_c = L_x L_y L_y$ is the volume of the continuous phase. Table 2.1 summarizes all the characteristic times involved, while Table 2.2 provides a detailed overview of all dimensionless parameters, their definitions, and the corresponding values used in the simulations.

Table 2.1 – Characteristic times existing in the present problem

Flow characteristic time	$t_{\text{flow}} = 1/\dot{\gamma}$
Droplet characteristic relaxation time	$t_{\text{drop}} = \eta r/\sigma$
Magnetic field characteristic time	$t_{\text{mag}} = \eta/\mu_0 \|\|\mathbf{H}_0\|\|^2$

Table 2.2 – Main dimensionless parameters of the problem.

Dimensionless parameter	**Definition**	**Values**
Reynolds number	$\text{Re} = \dfrac{\rho \dot{\gamma} r^2}{\eta_c}$	fixed: $\text{Re} = 0.01$
Viscosity ratio	$\lambda = \dfrac{\eta_d}{\eta_c}$	fixed: $\lambda = 1$
Density ratio	$\rho = \dfrac{\rho_d}{\rho_c}$	fixed: $\rho = 1$
Magnetic permeability ratio	$\zeta = \dfrac{\mu_d}{\mu_0}$	fixed: $\zeta = 2$
Capillary number	$\text{Ca} = \dfrac{t_{\text{drop}}}{t_{\text{flow}}} = \dfrac{\eta_c r \dot{\gamma}}{\sigma}$	variable
Magnetic capillary number	$\text{Ca}_{\text{mag}} = \dfrac{t_{\text{drop}}}{t_{\text{mag}}} = \dfrac{\mu_0 r \\|\mathbf{H}_0\\|^2}{\sigma}$	variable
Volume fraction of droplets	$\Phi = \dfrac{N V_d}{V_c}$	variable

3 Numerical methodology

3.1 Level-set method

In problems involving an interface that separates two or more phases, several tracking or capturing techniques can be employed for numerical description, including the boundary integral method, smoothed particle hydrodynamics, immersed boundary methods, level set (LS) method, volume of fluid, among others. In this work, we adopt the capturing method based on the level set formulation introduced by Osher and Sethian (1988).

The level set method is a powerful tool for topology optimization of shapes. It is well-established in the literature, and there have been a large number of papers published for over a decade using this method to analyze a wide range of problems. For example, Sussman et al. (1994) studied the motion of air bubbles in water and falling water drops in air, while Xu et al. (2006) and Pimenta and Oliveira (2021) worked with surfactant-covered droplets. Bashir et al. (2011) and Wong et al. (2017) analyzed droplet formation in a microfluidic T-junction. Moreover, Amani et al. (2019) investigated the deformation of a single droplet in shear flow, while Cunha et al. (2018) and Abicalil (2021) extended this idea to ferrofluid droplets subjected to both shear flow and external magnetic fields.

Let us consider Ω_c and Ω_d as the regions occupied by each of the two phases, where the subscript c corresponds to the continuous phase and d to the dispersed phase. The LS function is defined across the entire computational domain $\Omega = \Omega_c \cup \Omega_d \cup \Gamma$. Within any arbitrary region, the closed interface Γ is represented by the level set function ϕ, which denotes the signed distance from points in Ω to Γ. As commonly used in the literature, the LS function assumes negative values inside the droplet, positive values outside, and zero on Γ, thereby the interface is a material surface. In addition, since the interface is time-dependent and subject to the *no-slip condition*, it evolves through an advective equation

$$\frac{\partial \phi}{\partial t} + \mathbf{u} \cdot \nabla \phi = 0, \tag{3.1}$$

where $\mathbf{u}(\mathbf{x},t)$ is the velocity field. Note that the gradient of ϕ is orthogonal to Γ, which allows us to define geometrical quantities such as the normal vector throughout the entire domain,

$$\hat{\mathbf{n}} = \frac{\nabla\phi}{|\nabla\phi|}, \tag{3.2}$$

and also the mean curvature

$$\kappa = \nabla\cdot\hat{\mathbf{n}}. \tag{3.3}$$

Moreover, the material properties are determined in terms of the LS function, including the viscosity and magnetic permeability in the two liquid phases, respectively, by:

$$\eta(\mathbf{x},t) = \eta(\phi(\mathbf{x},t)), \tag{3.4}$$

$$\mu(\mathbf{x}) = \mu(\phi(\mathbf{x},t)). \tag{3.5}$$

The difference in properties between the droplets and the carrier fluid causes a stress jump at the interface, which leads to numerical instabilities. To avoid this abrupt discontinuity, we use a smoothed Heaviside function given by

$$\mathcal{H}_\epsilon(\phi) = \begin{cases} 0 & \text{if } \phi < -\epsilon, \\ \dfrac{1}{2}\left[1 + \dfrac{\phi}{\epsilon} + \dfrac{1}{\pi}\sin\left(\dfrac{\pi\phi}{\epsilon}\right)\right] & \text{if } -\epsilon \le \phi \le \epsilon, \\ 1 & \text{if } \phi > \epsilon, \end{cases} \tag{3.6}$$

where the interface has a finite thickness ϵ that is larger than the spacing between mesh points. In this work, we set $\epsilon = 1.5h$, where h is the mesh spacing, as done by Abicalil (2021). Thus, the proprieties of equations (3.4) and (3.5) are replaced by smooth transitions as

$$\lambda(\phi) = \lambda + (1-\lambda)\mathcal{H}_\epsilon(\phi) \tag{3.7}$$

$$\zeta(\phi) = \zeta + (1-\zeta)\mathcal{H}_\epsilon(\phi). \tag{3.8}$$

By definition, the directional derivative of the Heaviside function in the normal direction is the Dirac delta function at points near the interface (Osher and Fedkiw, 2006)

$$\delta(\mathbf{x}-\mathbf{x}_\Gamma) = \nabla\mathcal{H}_\epsilon(\phi(\mathbf{x}))\cdot\hat{\mathbf{n}}. \tag{3.9}$$

Using the chain rule, we have that:

$$\nabla \mathcal{H}_\epsilon(\phi(\mathbf{x})) \cdot \hat{\mathbf{n}} = \mathcal{H}'_\epsilon \nabla\phi \cdot \hat{\mathbf{n}} = \mathcal{H}'_\epsilon \nabla\phi \cdot \frac{\nabla\phi}{|\nabla\phi|} = \mathcal{H}'_\epsilon |\nabla\phi|. \tag{3.10}$$

Thus, knowing that $\mathcal{H}'_\epsilon(\phi) = \delta_\epsilon(\phi)$ the equation (3.10) reduces to $\delta(\mathbf{x} - \mathbf{x}_\Gamma) = \delta_\epsilon(\phi)|\nabla\phi|$ and is used in the capillary term of the momentum balance equation to accurately concentrate the stresses in the problem formulation with a smoothed Dirac delta function.

As introduced by Peng et al. (1999), we use a tubes technology, which involves creating a region γ near the interface, ensuring that ϕ is updated over time only in this local region (red region in Figure 3.1). In the FENRir code, we set $\gamma = 6\max(\Delta x, \Delta y, \Delta z)$, and in every region where $|\phi(\mathbf{x})| < \gamma$ the variable Tubes is equal to 2. At the borders of the tubes, where $|\phi(\mathbf{x} + \Delta\mathbf{x})| < \gamma$, the value changes as it moves less than one grid point. Moreover, we create a tube near the wall to use a repulsive force and prevent droplet-wall contact, as detailed in the Section 3.6.

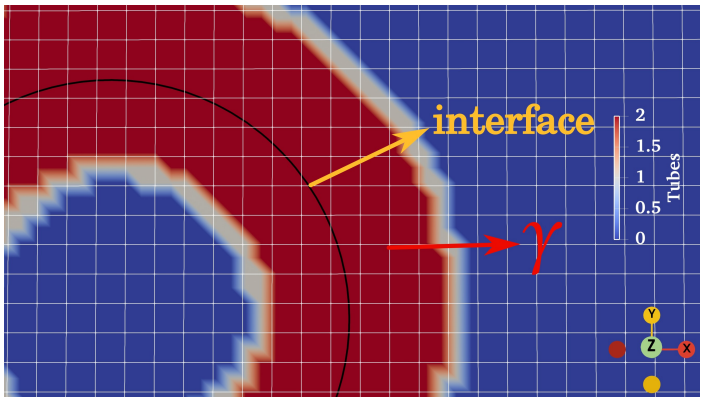

Figure 3.1 – Tube region and cross section of a drop interface from a real simulation.

We incorporated a cut-off function to smooths the LS function transport equation within the tube bands, reducing numerical oscillations. Thus, equation (3.1) is rewritten as:

$$\frac{\partial\phi}{\partial t} + c(\phi)\mathbf{u} \cdot \nabla\phi = 0, \tag{3.11}$$

where

$$c(\phi) = \begin{cases} 1 & \text{if } |\phi| \leq \beta, \\ \dfrac{(|\phi| - \gamma)^2(2|\phi| + \gamma - 3\beta)}{(\gamma - \beta)^3}, & \text{if } \beta < |\phi| \leq \gamma, \\ 0 & \text{if } |\phi| > \gamma. \end{cases} \tag{3.12}$$

Here, β is a more internal region than γ, defined by the points where $|\phi| \leq \beta$, given by $\beta = 3\max(\Delta x, \Delta y, \Delta z)$. As the interface moves, the level set function may not remain as a distance function throughout the simulation, thus we use a reinitialization technique, as done by Osher and Fedkiw (2006)

$$\frac{\partial \phi}{\partial \tau} + S(\phi)(|\nabla \phi| - 1) = \lambda_r \delta(\phi)|\nabla \phi|, \tag{3.13}$$

where $S(\phi)$ is the sign function, τ is a virtual time, and λ_r is a parameter to preserve the volume during the reinitialization, see Abdo et al. (2023) for further details. Equation (3.13) must satisfy $|\nabla \phi| = 1$, meaning it should evolve for a virtual time until this condition is holds, ensuring that the ϕ represents the distance function.

3.2 Surface and volume integrals

By employing the Heaviside and Dirac delta functions, we can obtain volume integrals in each phase for an arbitrary function $\mathcal{F}$ as follows:

$$\int_{\Omega_c} \mathcal{F} dV = \int_V \mathcal{F}\mathcal{H}_\epsilon(\phi) dV, \quad \int_{\Omega_d} \mathcal{F} dV = \int_V \mathcal{F}\mathcal{H}_\epsilon(-\phi) dV, \tag{3.14}$$

$$\int_\Gamma \mathcal{F} dS = \int_V \mathcal{F}\delta_\epsilon(\phi)|\nabla \phi| dV. \tag{3.15}$$

Equations (3.15) and (3.14) are numerically evaluated using a second-order quadrature with a 27-point cubic stencil. These integrals are crucial for computing various properties, such as the centroids and moments of inertia of the dispersed phase drops. As the drops move through the periodic domain, the centroid needs to be continuously adapted. The specific procedure is outlined in Algorithm 1.

Algorithm 1: The complement of centroid calculation for periodic domain

if $x_{center\_droplets}(N) > Lx$ **then**
  $x_{\text{center\_droplets}}(N) \leftarrow x_{\text{center\_droplets}}(N) - Lx$
end
else if $x_{center\_droplets}(N) \leq 0.0$ **then**
  $x_{\text{center\_droplets}}(N) \leftarrow x_{\text{center\_droplets}}(N) + Lx$
end
To calculate the moment of inertia
$xc \leftarrow x(i,j,k) - dx/2 - x_{\text{center\_droplets}}(N)$
$post \leftarrow xc - 0.5(1.0 - \text{sign}(1.0, 1.0 - \text{abs}(xc)/(Lx/2)))\text{sign}(1.0, xc)Lx$

3.3 Projection method

The projection method is a classical scheme for solving the incompressible Navier-Stokes equations. It involves decoupling the velocity and pressure variables by introducing artificial compressibility in a way that does not affect the final results. This is necessary because we do not have an explicit equation for pressure, unlike compressible flows, where pressure is a thermodynamic property determined by an equation of state. Thus, the projection method follows multi-step process. Firstly, the incompressibility condition and the pressure gradient terms are neglected, and a prediction velocity $\hat{\mathbf{u}}$ is calculated. In the second part, this velocity is used to compute an auxiliary variable for the pressure $\mathcal{P}$, and finally, the pressure and velocity fields are corrected, satisfying the incompressibility condition.

In this work, to achieve second order accuracy in time $\mathcal{O}(\Delta t^2)$, we use the second-order-explicit Adams-Bashforth scheme for the convective terms and the second-order-implicit Crank-Nicholson for the viscous terms. Assuming a single value for the viscosity ratio throughout the entire simulation, as described by Kim and Moin (1985), the steps of this method are as follows

$$\frac{\hat{\mathbf{u}}-\mathbf{u}^n}{\Delta t} = -(\mathbf{u}\cdot\nabla\mathbf{u})^{n+1/2} + \frac{1}{2Re}\left(\nabla^2\hat{\mathbf{u}} + \nabla^2\mathbf{u}^n\right) - \frac{1}{CaRe}\left[\kappa(\phi)\delta(\phi)|\nabla\phi|\hat{\mathbf{n}}\right]^{n+1/2} + \frac{Ca_{mag}}{CaRe}\left[\left(\zeta(\phi)-1\right)\mathbf{H}\cdot\nabla\mathbf{H}\right]^{n+1/2}, \tag{3.16}$$

$$\frac{\mathbf{u}^{n+1}-\hat{\mathbf{u}}}{\Delta t} = -\nabla\mathcal{P}^{n+1}, \tag{3.17}$$

where Δt is a time step. The terms at $n+1/2$, including the advective, capillary, and magnetic terms, as well as the term at $n+1$, are extrapolated of the form

$$(\mathbf{u}\cdot\nabla\mathbf{u})^{n+1/2} = \frac{3}{2}(\mathbf{u}\cdot\nabla\mathbf{u})^{n} - \frac{1}{2}(\mathbf{u}\cdot\nabla\mathbf{u})^{n-1} \tag{3.18}$$

$$\mathbf{u}^{n+1} = 2\mathbf{u}^{n} - \mathbf{u}^{n-1}. \tag{3.19}$$

By applying the divergence to equation (3.17) and noting that the velocity term at $n+1$ becomes zero due to incompressibility, we obtain the following Poisson equation for the pressure auxiliary variable:

$$\nabla^2\mathcal{P}^{n+1} = \frac{1}{\Delta t}\nabla\cdot\hat{\mathbf{u}}. \tag{3.20}$$

After solving equation (3.20) and calculating $\mathbf{u}^{n+1}$ using equation (3.17), the pressure field can be determined as

$$p^{n+1} = \mathcal{P}^{n+1} - \frac{1}{2Re}\nabla\cdot\hat{\mathbf{u}}. \tag{3.21}$$

3.4 Discretization and linear system of equations

In this work, the governing equations are solved on a three-dimensional uniform Cartesian mesh using the second-order finite difference method. Moreover, the mesh is staggered; thus, the components vector variables are located at the cell faces (velocity, magnetic potential, etc.), and the scalar variables are located on center of the grid cells (pressure, level set function, etc.).

The advective terms present in the Navier-Stokes equations, the transport equation of the level set function, and its reinitialization equation are formulated using the upwind scheme. Thus, it is important to use higher-order methods for spatial discretization when calculating derivatives. For the terms in equation (3.16), we use a second-order essentially non-oscillatory (ENO) scheme, which provides better numerical approximations. The idea is to compute numerical flux functions using the smoothest polynomial interpolants possible. To calculate the derivatives of the advective terms in the transport equation of the LS function, it is important to use an order higher than two, due to the significant numerical error caused by

mass loss of the droplet. Therefore, according to Osher and Fedkiw (2006), we use a fifth-order weighted essentially non-oscillatory (WENO) scheme, which employs the points $\{\phi_{i-2},\phi_{i-1},\phi_i,\phi_{i+1},\phi_{i+2},\phi_{i+3}\}$ in the x-direction, for example. Note that this scheme is a weighted average of all the values obtained by an ENO scheme. For the spatial discretization in the reinitialization algorithm, we use the upwind scheme along with WENO and Godunov for computing ϕ_x^- and ϕ_x^+.

For the time evolution of the LS transport and reinitialization equation, where explicit methods are adopted for temporal discretization, we employ a third-order strong stability preserving (SSP) Runge-Kutta scheme, as recommended by Peng et al. (1999) when using fifth-order WENO. As mentioned in Section 3.3, the Navier-Stokes equations are temporally discretized using second-order implicit Crank-Nicolson and also Adams-Bashforth schemes.

Based on the previous schemes shown, equations (3.16), (3.20), and (2.31) are discretized to form linear systems for velocity, pressure, and magnetic potential. For example, the discretization of the equation for the magnetic potential, considering only the x-components, is given by

$$\frac{\partial}{\partial x}\left(\zeta(\phi)\frac{\partial \psi_{\mathrm{P}}}{\partial x}\right)^{n+\frac{1}{2}} = \frac{\partial}{\partial x}\left(\zeta(\phi)\right)^{n+\frac{1}{2}} H_{0x}. \tag{3.22}$$

The derivative is approximated with second-order accuracy and defined at the midpoint between two grid points

$$\frac{\zeta(\phi)_{i+\frac{1}{2},j,k}\left(\frac{\psi_{i+1,j,k}-\psi_{i,j,k}}{\Delta x}\right)-\zeta(\phi)_{i-\frac{1}{2},j,k}\left(\frac{\psi_{i,j,k}-\psi_{i-1,j,k}}{\Delta x}\right)}{\Delta x} = \frac{\zeta(\phi)_{i+\frac{1}{2},j,k}-\zeta(\phi)_{i-\frac{1}{2},j,k}}{\Delta x} H_{0x} \tag{3.23}$$

We use a harmonic mean in the discretization of $\zeta(\phi)_{i+1/2,j,k}$,

$$\zeta(\phi)_{i+1/2,j,k} = \frac{2}{\frac{1}{\zeta(\phi)_{i+1,j,k}}+\frac{1}{\zeta(\phi)_{i,j,k}}}. \tag{3.24}$$

Equation (3.23) can be reewriten as

$$\frac{1}{\Delta x^2}\Big[\zeta(\phi)_{i+\frac{1}{2},j,k}\psi_{i+1,j,k}+\zeta(\phi)_{i-\frac{1}{2},j,k}\psi_{i-1,j,k} - (\zeta(\phi)_{i+\frac{1}{2},j,k}+\zeta(\phi)_{i-\frac{1}{2},j,k})\psi_{i,j,k}\Big] = \frac{\zeta(\phi)_{i+\frac{1}{2},j,k}-\zeta(\phi)_{i-\frac{1}{2},j,k}}{\Delta x}H_{0x}. \tag{3.25}$$

Rearranging and grouping the terms, we obtain the following coefficients

$$a_{i,j,k} = \frac{\zeta_{i-1/2,j,k}}{\Delta x^2}, \tag{3.26}$$

$$b_{i,j,k} = \frac{\zeta_{i,j-1/2,k}}{\Delta y^2}, \tag{3.27}$$

$$c_{i,j,k} = \frac{\zeta_{i,j,k-1/2}}{\Delta z^2}, \tag{3.28}$$

$$d_{i,j,k} = -\left(\frac{\zeta_{i-1/2,j,k}+\zeta_{i+1/2,j,k}}{\Delta x^2}+\frac{\zeta_{i,j-1/2,k}+\zeta_{i,j+1/2,k}}{\Delta y^2}+\frac{\zeta_{i,j,k-1/2}+\zeta_{i,j,k+1/2}}{\Delta z^2}\right), \tag{3.29}$$

$$e_{i,j,k} = \frac{\zeta_{i+1/2,j,k}}{\Delta x^2}, \tag{3.30}$$

$$f_{i,j,k} = \frac{\zeta_{i,j+1/2,k}}{\Delta y^2}, \tag{3.31}$$

$$g_{i,j,k} = \frac{\zeta_{i,j,k+1/2}}{\Delta z^2}, \tag{3.32}$$

$$h_{i,j,k} = \frac{\zeta(\phi)_{i+\frac{1}{2},j,k}-\zeta(\phi)_{i-\frac{1}{2},j,k}}{\Delta x}H_{0x}+\frac{\zeta(\phi)_{i,j+\frac{1}{2},k}-\zeta(\phi)_{i,j-\frac{1}{2},k}}{\Delta y}H_{0y} \tag{3.33}$$

$$+\frac{\zeta(\phi)_{i,j,k+\frac{1}{2}}-\zeta(\phi)_{i,j,k-\frac{1}{2}}}{\Delta z}H_{0z}. \tag{3.34}$$

Then we form a linear system with variable coefficients for the magnetic potential as

$$a_{i,j,k}\psi_{i-1,j,k}+b_{i,j,k}\psi_{i,j-1,k}+c_{i,j,k}\psi_{i,j,k-1}+d_{i,j,k}\psi_{i,j,k}+e_{i,j,k}\psi_{i+1,j,k}+ f_{i,j,k}\psi_{i,j+1,k}+g_{i,j,k}\psi_{i,j,k+1}=h_{i,j,k}. \tag{3.35}$$

3.5 Boundary and initial conditions

The boundary and initial conditions applied to the problem are described below:

- The drops are initially spherical and homogeneous with a unit radius. They are randomly distributed by a random number generator;
- In the x and z directions, the magnetic potential is periodic, while it has Neumann boundary conditions in the y direction;
- Velocities and pressure fields are periodic in the x and z directions.
- The pressure field has homogeneous Neumann conditions at the walls;
- Non-homogeneous Dirichlet boundary conditions are applied to $\mathbf{u}$ at the non-periodic boundaries, corresponding to the impenetrability and no-slip conditions.

3.6 Repulsive force model

In emulsions, coalescence occurs when the interfacial film between the surface of droplets becomes thin and breaks. Droplets approach each other, irreversibly merge, and form larger droplets until the liquid phases completely separate. The macroscopic properties change with the merging or breaking up of droplets. To avoid this unstable scenario, repulsive forces in numerical simulations play a crucial role, especially because it is very difficult to numerically resolve the flow in the narrow gaps between closely spaced droplets. Therefore, we use a repulsive force model as proposed by De Vita et al. (2019),

$$\mathbf{F}_{rep} = \eta_c r U \left(\frac{a}{\phi} + \frac{b}{\phi^2} \right) \hat{\mathbf{n}}, \tag{3.36}$$

where η_c is the viscosity of the base fluid, r is the droplet radius, U is a characteristic flow velocity, and a and b are calibration parameters. The first parameter can be interpreted as a contribution from long-range forces, while the second represents a short-range force. Figure 3.2a shows the system without any repulsive force, while

Figure 3.2b shows it with repulsive force between the droplets. Note that in Figure 3.2b, the topology of the droplets did not undergo an irreversible change and the initial number of droplets remained the same.

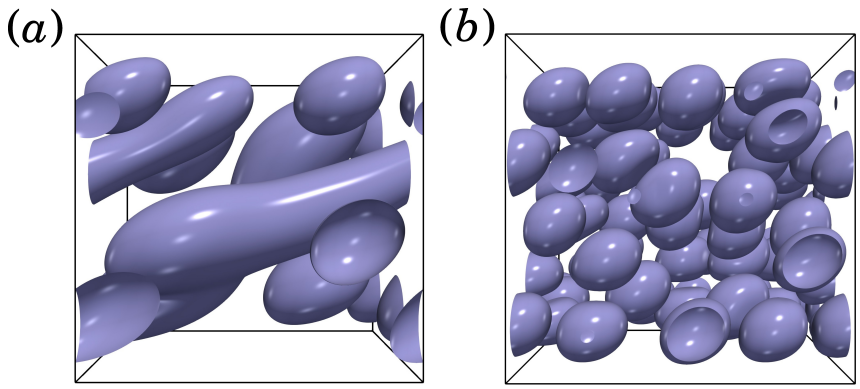

Figure 3.2 – Snapshots of the simulated domain without repulsive force (a) and with repulsive force(b). Both simulations started with the same number of droplets for $\Phi = 0.25$, $\mathrm{Re} = 0.01$ and $Ca = 0.05$.

To correctly compute the repulsive force, we first attribute an identity (Id) to each droplet through the level set function. This means that each droplet is identified by a corresponding integer ranging from 1 to the total number of droplets. Moreover, the Id is updated as ϕ evolves. Algorithm 2 describes this scheme. First, we define a temporary identifier Id_{temp}. Then, we introduce a conditional statement based on the variable ϕ (defined throughout the domain). If the value of ϕ is greater than 1 it means that we are outside the drop and thus we leave the loop without doing anything. Otherwise, if the value of ϕ is less than 1 and Id_{temp} is equal to 0, we sweep 1 stencil through the Id_{temp} and check if this variable identifies any values different from 0. If such a value is found, this means that the drop has moved and thus Id receives the value of the temporary variable, updating it.

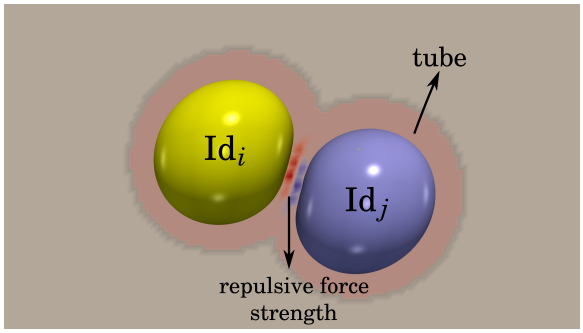

Figure 3.3 – Computational domain where two droplets are close enough for the repulsive force to be computed.

Algorithm 2: update Id

```
Id_temp = Id
if φ > 0 then
    Id = 0
end
else if φ ≤ 0 and Id_temp = 0 then
    Check the neighboring points (stencil of 1)
    if Id_temp at any neighboring point ≠ 0 then
        Id ← Id_temp at the neighboring point
    end
end
```

Through the Id variable, it is possible to determine if two droplets are close enough for the repulsive force to be activated. Inside the Tube that encompasses the region $|\phi| < \gamma$, where $\gamma = 6\max(\Delta x, \Delta y, \Delta z)$, we check within a $3\Delta x \times 3\Delta y \times 3\Delta x$ stencil if there are two Id values. If there are, the repulsive force is computed, as shown in Figure 3.3. We add an Id to the walls normal to the y-axis, so the repulsive force is also computed when droplets are nearby, preventing mass loss. Algorithm 3 describes how we implement the repulsive force.

Algorithm 3: repulsive force

```
if tubes then
    Repulsive force=.false. ;        /* search the first non-zero Id  */
    if Id ≠ 0 then
        Id_ first ← Id
    end
    Check the neighboring points (stencil of 3)
    if Id ≠ 0  and  Id ≠ Id_first then
        Repulsive force=.true.
    end
end
```

To evaluate the repulsive force algorithm, we simulate two spherical droplets of identical size, each with a unit radius r. Both are positioned in a cubic computational domain of size $L_x = 12r$, $L_y = 6r$, and $L_z = 6r$. At time zero, the offsets between the two droplets are $\Delta x = -3$, $\Delta y = 1.5$ e $\Delta z = 0$. This setup is similar to that in De Vita et al. (2019). Figure 3.4 shows a plot of the relative y displacement as a function of the relative x displacement between the centroids of the droplets. First of all, we check the influence of mesh refinement on the interaction between the two droplets without repulsive force. We start by using a mesh of $192 \times 96 \times 96$ cells (dashed line) and then double this to $384 \times 192 \times 192$ cells (solid line). Note that, in the initial moments, the droplets are not in apparent contact, so the relative vertical distance remains constant. However, when they start to interact, Δy increases and then suddenly decreases drastically for both the dashed and solid lines without the repulsive force. This indicates that, with greater computational power and finer mesh refinement, the droplets probably would not coalesce, just as predicting De Vita et al. (2019), despite them using the finite volume method. The solid line achieves a longer simulation time compared to the dashed line, which has half the mesh refinement. This indicates that with higher computational power and further mesh refinement, the droplets probably would not coalesce. The dashed curve comes from our simulation with repulsive force, using coefficient values $a = 55$ and $b = 3.5$, the same values used by De Vita et al. (2019) in all their results with repulsive force summarized in the dotted curve. Note that the repulsive force model effectively prevents droplet merging. At first, Δy starts to increase when the droplets are very close, reaches a maximum, and then, after separation, returns to a new constant vertical displace-

ment value until the next collision.

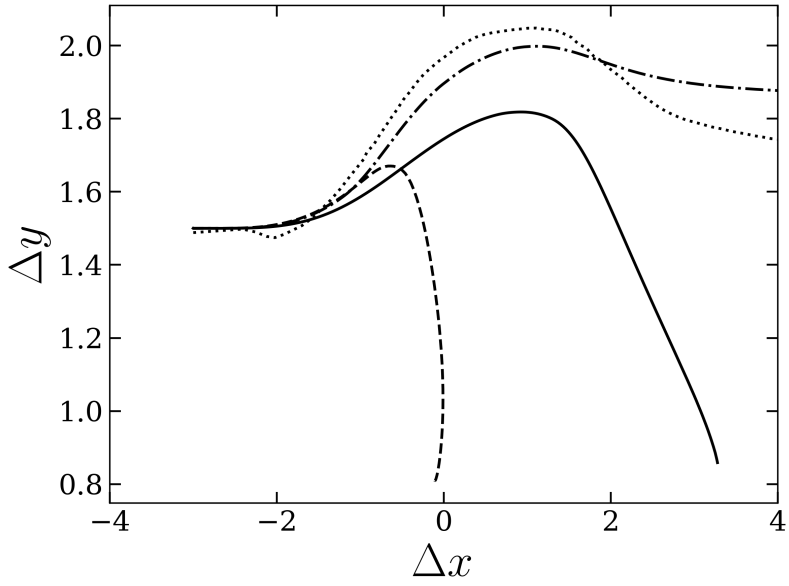

Figure 3.4 – Relative trajectories of two droplets interacting in shear flow. The dashed, solid, and dash-dot lines are curves from our simulations using the level set method for $Ca = 0.1$ and $Re = 0.01$. The solid line has double the resolution of the dashed line, and both are without repulsive force. The dash-dot line includes a repulsive force with parameters $a = 55$ and $b = 3.5$, similar to the dotted line from De Vita et al. (2019) for $Ca = 0.1$ and $Re = 0.1$ using VoF. The viscosity and density ratios in both works are equal to unity.

A comparison with the experimental work of Guido and Simeone (1998) is performed. We established an initial configuration of the droplets with a vertical distance of $\Delta y = 0.43$ between the centers, for $Ca = 0.13$, $\lambda = 1.4$, and $Re = 0.01$. The domain has dimensions $L_x = L_y = L_z = 10r$, with a uniform grid of $160 \times 160 \times 160$. Figure 3.5 shows Δy as a function of Δx. We conducted two simulations with different intensities of the repulsive force. The dashed curve has coefficients $a = 55$ and $b = 3.5$ for equation (3.36), while the solid line has values $a = 0$ and $b = 3.0$. The curve with open circles is from Guido and Simeone (1998). The droplets approach, reach a maximum relative distance in y, and then move apart. At all these moments, the solid curve aligns better with the experimental curve because it has a lower intensity repulsive force compared to the dashed curve case. However, note that for both cases, the final net relative displacement of the two droplets is significantly higher than in the experimental cases. Figure 3.6 shows some plots at different instances of the solid curve from Figure 3.5, illustrating how droplets interact with a repulsive

force (right column) and without a repulsive force (left column). Even though the repulsive force effectively prevents droplet merging, it does not fully capture the real behavior of the interaction between two or more droplets in a flow. It is an artificial force modeled solely to prevent coalescence in numerical simulations. However, when analyzing the bulk response of the system, it proves effective, as we will discuss later on. Moreover, the difference between the initial and final Δy values occurs due to a breakdown in flow symmetry caused by conditions of kinematic irreversibility. In our case, it is the particle deformation, which leads to a self-diffusive phenomenon (Loewenberg and Hinch, 1997).

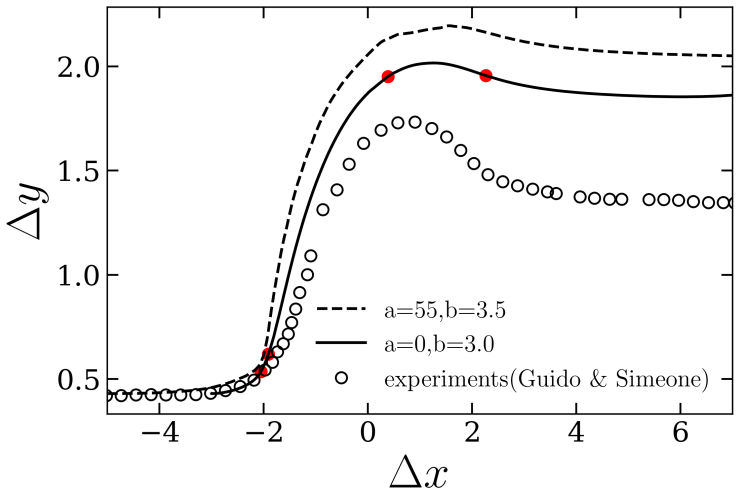

Figure 3.5 – Relative trajectories of two droplets interacting in shear flow. Comparing our collision force results, represented by dashed and solid lines, with those obtained from the experimental results (open circles) by Guido and Simeone (1998). We set $Ca = 0.135$, $\lambda = 1.37$, and $Re = 0.01$. The red points are the time instants corresponding to the plots in Figure 3.6.

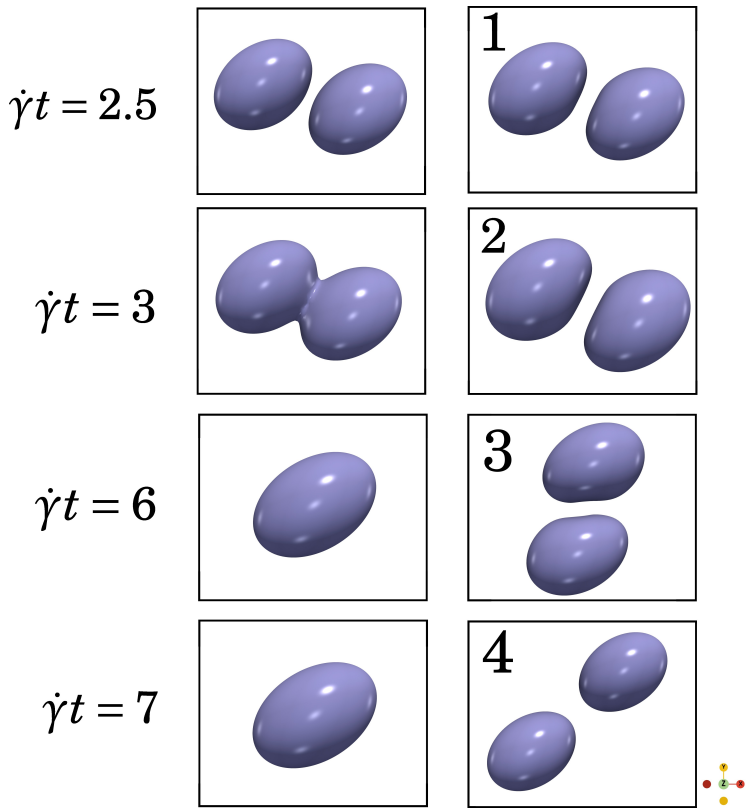

Figure 3.6 – Sequences of the trajectories of two droplets interacting in shear flow over time. The left column shows a simulation without repulsive force, while the right column includes the repulsive force. The frames on the right correspond to different time instants indicated by red circles on the curve in Figure 3.5. Plot number 1 represents the earliest time instant indicated by the first circle, and so on.

As the relative net displacement between two droplets changes according to the intensity of the repulsive force, we simulated different values of the calibration parameters for this force using the same setup as depicted in Figure 3.5. Figure 3.7(a) shows the relative trajectory between the droplets. For $a = 0$ and $b = 1.5$ (yellow curve with cross symbols), the applied force was not sufficient, and the droplets merged. On the other hand, there was no merging for $a = 5$, $b = 1.5$, as well as for $a = 0$, $b = 3.0$, and $a = 10$, $b = 1.5$. These three cases exhibited similar final vertical displacements, as shown in the insets of Figure 3.7(a). We chose the values $a = 0$ and $b = 3.0$ for all simulations in this work, except when $Ca = 0.05$, where the tendency for coalescence is greatest, we used $a = 55$ and $b = 3.5$ (red line with square symbols). Figure 3.7(b) shows the minimum distance between the interfaces of two droplets over time for two different intensities of collision forces. This minimum distance is calculated using the closest point method, previously developed by our group and further ex-

plained in the paper by Pimenta and Oliveira (2021). The initial simulation setup is the same as in the previous case. At the initial time, the droplets are not in contact, and the curves remain overlapping and decrease linearly until contact. At this point, the curves differ because the influence of repulsion is different in each case. For $a = 0$ and $b = 3.0$, the minimum distance during contact is smaller, and the shapes of the droplets are more symmetric and uniform. Conversely, for $a = 55$, the curvature inverts for both droplets due to the high repulsion force applied. The non-smoothness at the end of the curve is due to mesh refinement, but the values do not fluctuate significantly.

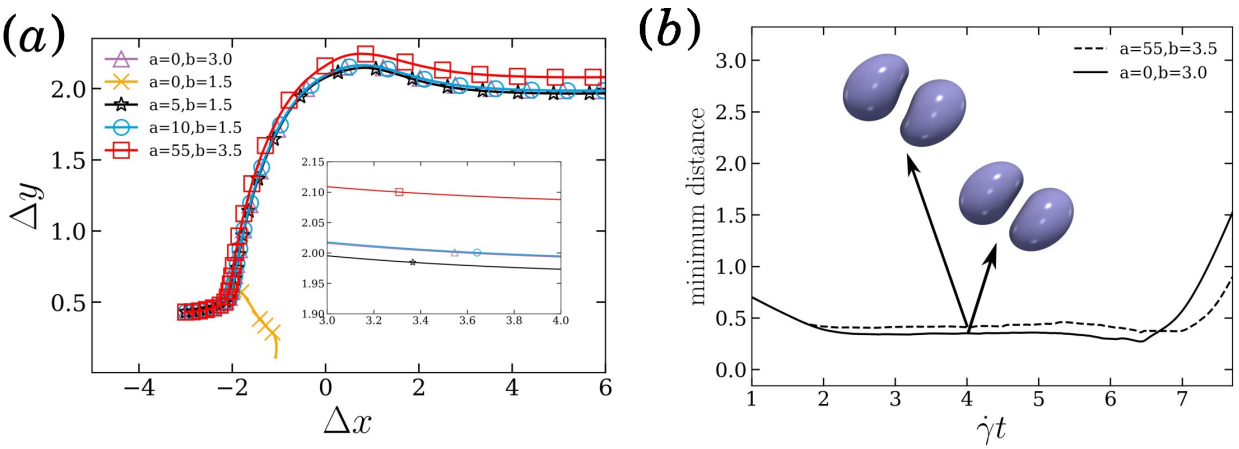

Figure 3.7 – (a) Relative trajectories between two droplets, Δy as a function of Δx, for different calibration parameters a and b. (b) Minimum distance between two droplets as a function of time for two different intensities of repulsive force. The inset in (a) shows further detail on the difference in final net relative displacement between the cases. We set $Ca = 0.135$, $\lambda = 1.37$, and $Re = 0.01$ for the tests.

In addition, while testing the collision force model from De Vita et al. (2019), we formulated a repulsive force to achieve greater similarity with lubrication theory. Instead of using a characteristic velocity, we proposed a model with the normal relative velocity between the droplets, such that the repulsive force is described as

$$\mathbf{F}_{\text{rep}} = 6\pi\eta_c r(\mathbf{u}\cdot\hat{\mathbf{n}})\left(\frac{a}{\phi}\right)\hat{\mathbf{n}}, \tag{3.37}$$

which, in dimensionless form, is rewritten as:

$$\mathbf{F}_{\text{rep}} = \frac{6\pi}{Re}(\mathbf{u}\cdot\hat{\mathbf{n}})\left(\frac{a}{\phi}\right)\hat{\mathbf{n}}. \tag{3.38}$$

This formulation was not tested in this work, but should be tested in future works.

3.7 Implementation and processing time

All simulations in this work were performed using the computational code FENRir (Ferrofluid Emulsion Numerical Rheometer), developed by the group in the Fortran 95 programming language. The Poisson equation for the pressure (equation (3.20)), which results in the linear system, is solved using the Fast Poisson Solver (FPS), as well as for the linear system resulting from the momentum equation (equation (3.16)). On the other hand, due to variable coefficients, the linear system for the magnetic potential (equation (3.35)) is solved using the conjugate gradient method with a multigrid cycle, known as V-Cycle, as a preconditioner. For more details, see Abicalil (2021), McAdams et al. (2010).

In general, direct simulations of a suspension of deformable particles in non-dilute cases have a high computational cost, as they simultaneously solve various differential equations to describe the behavior of the particles in the system. Moreover, obtaining reliable values of properties based on statistical analysis requires a long simulation time. A time step of 10^{-3} is used in all cases. Most of the simulations were performed on an Intel(R) Xeon(R) CPU E5-2660 v4 2.00 GHz processor and took, on average, 15 days to reach $\dot{\gamma}t = 35$, which is the time when the mean properties of the system reaches an apparent steady state.

4 Results and discussions

This chapter presents the results and discussions of the performed numerical simulations, divided into three parts. The first part analyzes mesh convergence. The second part investigates a monodispersed ferrofluid emulsion under shear flow in the absence of a magnetic field, where we determine the shear viscosity for different capillary numbers and volume fractions of the droplets and compare the results with previous experimental, theoretical, and numerical works to validate our simulation. Finally, the third part examines the influence of the magnetic field on the viscosity, deformation, and orientation of the droplets. Moreover, we determine the bulk magnetic properties. For this purpose, we set three different volume fractions of the dispersed phase, $\Phi = \{0.10, 0.20, 0.30\}$, and simulated them for different capillary numbers, $Ca = \{0.05, 0.10, 0.20\}$, and magnetic capillary numbers. All simulations are conducted at a fixed Reynolds number, $\mathrm{Re} = 0.01$, a viscosity ratio, $\lambda = 1$, a magnetic permeability ratio, $\zeta = 2$, and a droplet radius, $r = 1$. Also, the system is neutrally buoyant. The number of droplets for each volume fraction is as follows: $\Phi = 0.10$ corresponds to 24 droplets, $\Phi = 0.20$ corresponds to 48 droplets, and $\Phi = 0.30$ corresponds to 72 droplets. We set a domain size of $10 \times 10 \times 10$, a grid spacing length of $h = 0.0625$, and a time step of $\Delta t = 10^{-3}$.

4.1 Mesh convergence

In this section, we investigate how our results respond to mesh refinement. To this end, we set up a representative case where $\Phi = 0.2$, which corresponds to 48 droplets placed in a cubic domain with dimensions $10 \times 10 \times 10$, $Ca = 0.1$, $\zeta = 2$, and $Ca_{mag} = 8$. We chose four different grids, namely $96 \times 96 \times 96$, $128 \times 128 \times 128$, $160 \times 160 \times 160$ and $192 \times 192 \times 192$. The total number of grid cells and the mesh size vary from $\sim 880,000$ to $\sim 7,000,000$ and from ~ 0.1 to ~ 0.05, respectively. Furthermore, due to the finite size of the domain and the small number of drops, wall effects may influence the overall dynamics of the system; however, this has not been further analyzed.

Figure 4.1 shows the effects of different grids on the average deformation of all

droplets over time. The deformation of each droplet is defined as

$$D_T = \frac{\ell - B}{\ell + B}, \tag{4.1}$$

where ℓ is the maximum and B is the minimum dimension of the drop. This measurement is based on the principal moments of inertia of the drops, obtained as the eigenvalues of the inertia tensor. Note that there are fluctuation due to drop-drop interactions. Hence, we determined the average of any property as the temporal average over a time interval in which the moving average remains stable, ignoring the initial transient part of the simulation. In other words, the results are calculated when the properties reach a approximately steady state. Under the assumptions of ergodicity, the temporal average of a physical quantity is equal to the ensemble average Moore (2015). The refinement leads to a convergence of the temporal average deformation of the droplets despite the fluctuations not following the exact same dynamics. This effect may be related to the random initial condition that results in a different distribution of droplets in each simulation, hence, the approach and separation between droplets are not the same in all cases. It may also be associated with a non-definitive steady state, as the applied magnetic field tends to orient the particles and form chains, while simple shear tends to break them, leading to a disordering of particle arrangements. Table 4.1 presents the effective viscosity, deformation, and bulk magnetization along with their respective errors. The errors are calculated as a temporal average of the standard deviations of the means at each time instant. Comparing the results of the first three grids to the last, which is the most refined tested, in terms of viscosity, we observe the following differences: 13.58%, 5.75%, and 1.087%, respectively, from the coarsest to the finest grid. In terms of bulk magnetization, there was no significant percentage variation in the results. However, for average deformation, the differences are 34.19%, 14.29%, and 4%. Therefore, we used a mesh $160 \times 160 \times 160$ of cells for all simulations, as it shows minimal differences in results and takes nearly half the simulation time compared to the most refined grid tested.

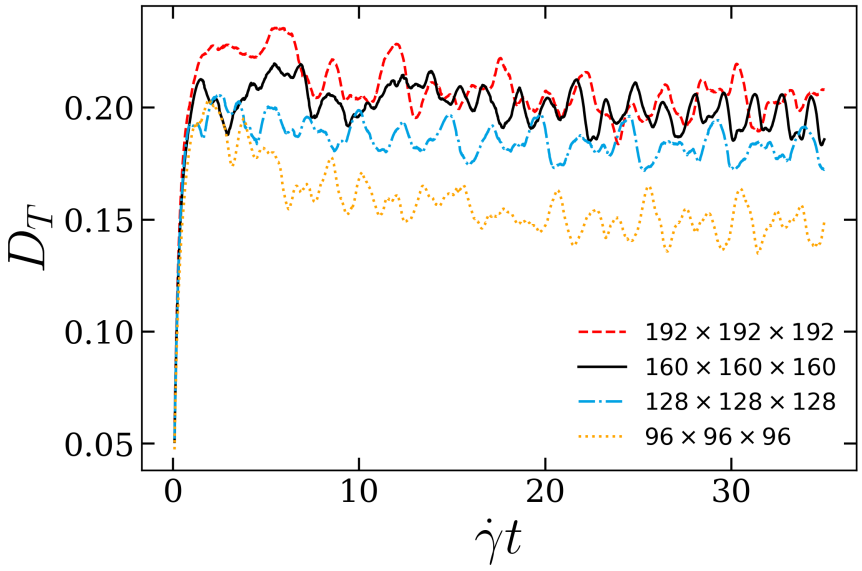

Figure 4.1 – Variation of average deformation with grid resolution for $\phi = 20\%$, $Re = 10^{-2}$, $Ca = 0.1$ and $Ca_{mag} = 8$.

Table 4.1 – Grid resolution test at $\phi = 20\%$, $Re = 10^{-2}$, $Ca = 0.1$ and $Ca_{mag} = 8$.

Grid resolution	h	η_{eff}/η_0	D_T	$\langle \mathbf{M} \rangle$
$96 \times 96 \times 96$	0.104	1.62 ± 0.014	0.155 ± 0.036	0.1458 ± 0.00023
$128 \times 128 \times 128$	0.078	1.74 ± 0.018	0.182 ± 0.029	0.1464 ± 0.00022
$160 \times 160 \times 160$	0.0625	1.84 ± 0.044	0.200 ± 0.037	0.1466 ± 0.00047
$192 \times 192 \times 192$	0.0521	1.86 ± 0.033	0.208 ± 0.046	0.1464 ± 0.00036

4.2 Non-magnetic emulsion in simple shear flow

In the absence of an external magnetic field, ferrofluid emulsions behave like typical emulsions. The viscosity is determined by equation (2.33) and shows fluctuations over time, which highlights the dynamic behavior of the system (see Figure 4.2). To achieve a steady state in a statistical sense, we calculate the bulk viscosity by taking a average starting from the moment when the moving average no longer varies significantly. In this context, Figure 4.3 shows the effective shear viscosity as a function of volume fraction of the droplets for the case of nearly spherical droplets at low Reynolds number, Ca = 0.05 and $\lambda = 1$. For a small droplets concentration,

the viscosity follows the Taylor equation (black dashed curve) for $\lambda = 1$, which describes the viscosity behavior of dilute suspensions ($\mathrm{Ca} \to 0$). This indicates that the interparticle interactions are negligible at low concentrations, and the viscosity behaves linearly with Φ. In contrast, for higher values of droplet volume fraction, the viscosity deviates significantly from the Taylor prediction. This deviation suggests that droplets interactions become increasingly important as the volume fraction increases, leading to higher stress. We compared our work using the level set method with that of Loewenberg (1998), which employs the boundary integral method. We found that the results agree quite well for similar parameters. Moreover, the dashed curve represents a theoretical result developed by Zinchenko (1984), which considers $\mathcal{O}(\Phi^2)$. This means it only accounts for interactions between two liquid spherical particles, so it deviates from the numerical work curves by not considering higher order volume fraction effects. The dash-dot curve shows an equation proposed by Pal (2001), based on experimental data covering a wide range of viscosity ratios.

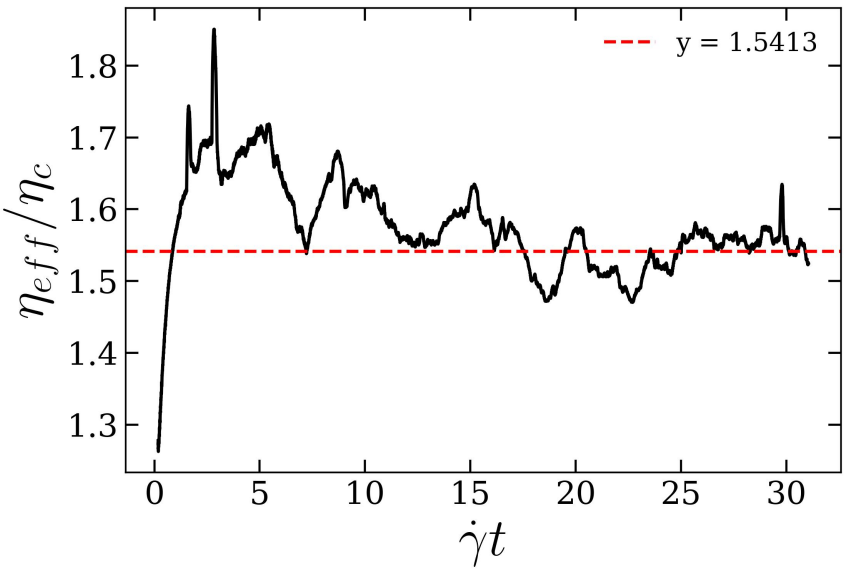

Figure 4.2 – Shear viscosity as a function of time for $\Phi = 0.30$, $Ca = 0.20$ and $Re = 0.01$. The red line corresponds to the average viscosity value calculated for this simulation.

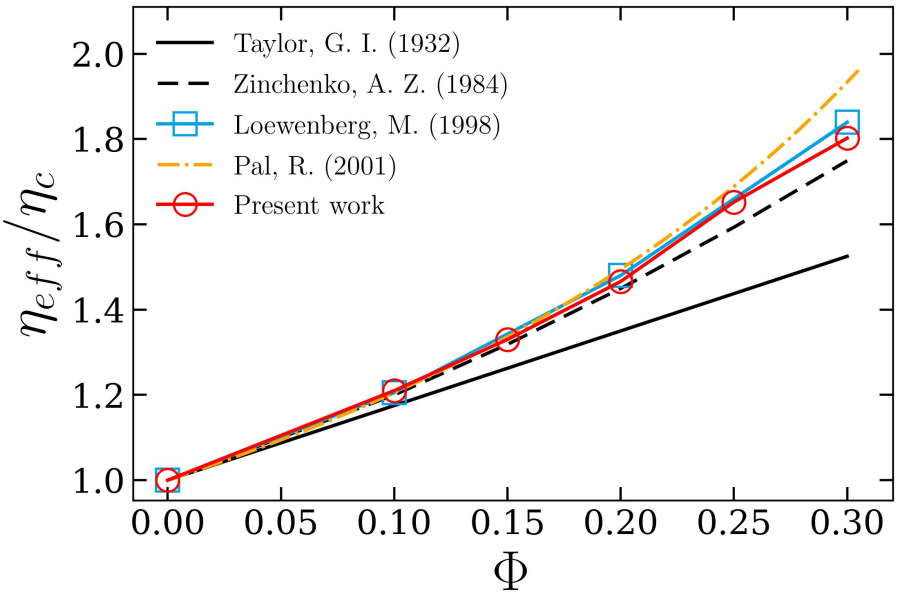

Figure 4.3 – Shear viscosity of the emulsion versus the volume fraction of the droplets at small Reynolds number. The black solid lines represents the Taylor's equation for the limit where $Ca \to 0$. The dashed line is a second-order approximation of effective viscosity developed by Zinchenko (1984). The orange dash-dotted line is Pal (2001) expression for the viscosity of concentrated emulsions of spherical droplets. The line with squares symbols is the work of Loewenberg (1998) using boundary integral method for $\mathrm{Ca} = 0.05$. The line with circles symbols is the present simulation using level set method at $\mathrm{Ca} = 0.05$, $\mathrm{Re} = 10^{-2}$ and $\lambda = 1$

Determining how the effective viscosity of an emulsion changes with an imposed shear rate is one of the most common ways to understand its rheological behavior. Figure 4.4 shows this relationship for different droplet concentrations. The circle symbols represent our numerical simulation results, while the square symbols come from the simulation performed by Loewenberg (1998) using the boundary integral method. These curves reveal a typical non-Newtonian behavior of emulsions. At low shear rates (and therefore low Ca), the droplets remain nearly spherical; this means that the relaxation time of the droplet is much shorter than the flow time. On the other hand, at higher shear rates, the flow time is short enough for us to observe significant changes in the shape of the drops. They stretch into a prolate shape due to the extensional component of the shear flow while rotating along the vorticity direction. As a consequence, the effective viscosity decreases (shear thinning). If we compare the case at $\Phi = 0.30$ (blue symbols) with that at $\Phi = 0.10$ (red symbols), we observe more pronounced shear thinning. Loewenberg and Hinch (1996)

point out that as the Φ increases, the droplets deform more and align more in the flow direction. Figure 4.5 show how droplets deform for different capillary numbers. Although our results agree well with those from the work using boundary integrals, our simulations predict droplet breakup at $Ca = 0.30$ and $\Phi = 0.30$ (see Figure 4.5(c)). This discrepancy is mainly explained by the fact that these two methods handle droplet breakup differently; our method deals better with abrupt topological changes. It means that the Level Set method represents the interface between different phases as an implicit surface defined by a level set function. This function can evolve over time smoothly and continuously, allowing direct capture of changes in interface topology. It has mechanisms to handle numerical singularities that may arise during abrupt changes in topology, such as interface collisions. This is facilitated by the continuous and differentiable nature of the level set function. On the other hand, the boundary integral method (BIM), while useful in many boundary value problems, may encounter difficulties in handling abrupt topological changes due to its approach of discretizing boundaries of a region. Abrupt changes may require redefining or adjusting boundaries, which is not always straightforward or efficient within the BIM framework. Therefore, Figures 4.3 and 4.4 demonstrate that our results exhibit the expected behavior according to previous research, leading to the conclusion that the repulsive force is being well computed.

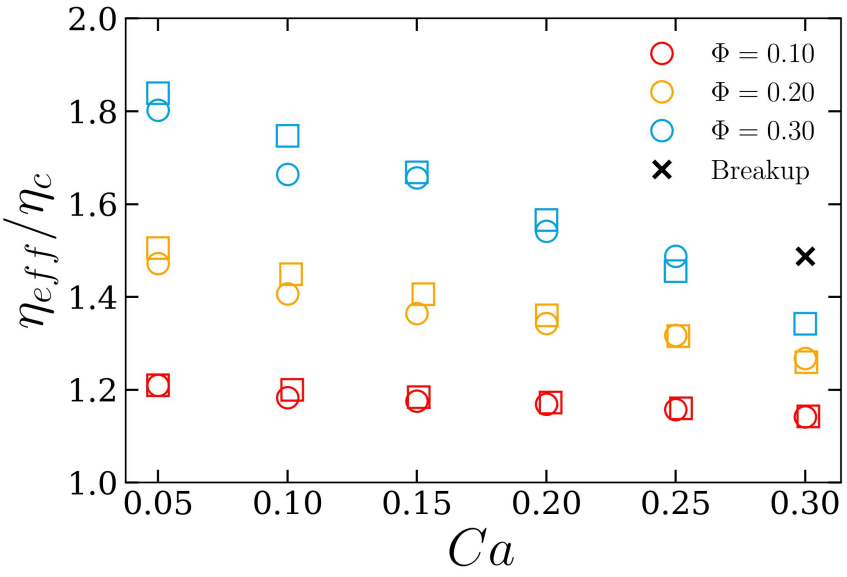

Figure 4.4 – Shear viscosity of the emulsion as a function of the capillary number for different values of the dispersed phase. The square symbols represent results from Loewenberg (1998), obtained using the boundary integral method. The circle and cross symbols represent our data, obtained with $Ca = 0.05$ and $Re = 0.01$.

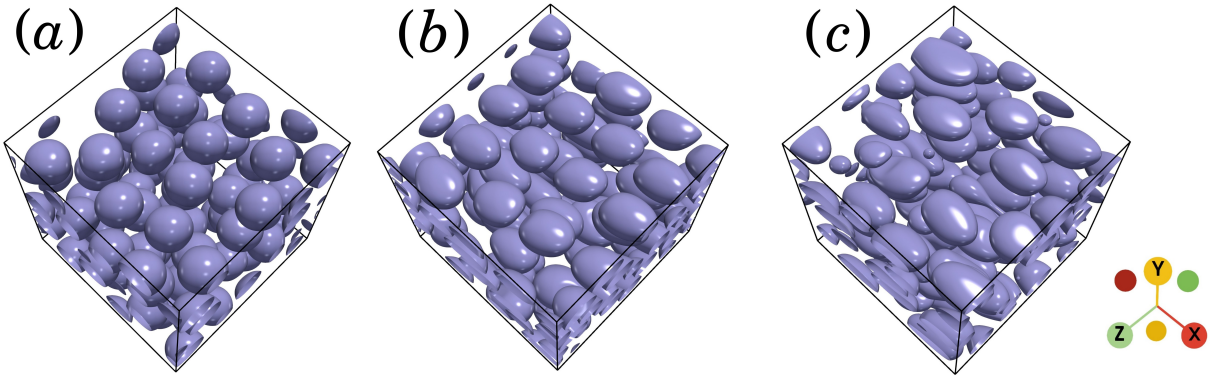

Figure 4.5 – Snapshots of the emulsion simulation for different capillary numbers: (*a*) Ca = 0.05, (*b*) Ca = 0.25 and (*c*) Ca = 0.30. All these numerical simulations were performed with the same Reynolds number Re = 0.01, viscosity ratio $\lambda = 1$, and volume fractions $\Phi = 0.30$.

4.3 Ferrofluid emulsion in simple shear flow

This section presents the influence of the external magnetic field, shear flow rate, and the droplet volume fraction on drop geometry, effective viscosity, bulk magne-

tization, the misalignment angle between $\mathbf{M}$ and $\mathbf{H}_0$, magnetic torque. The results discussed hereafter are obtained using a repulsive force with coefficients $a = 0$ and $b = 0.3$ for $\mathrm{Ca} = 0.1$ and $\mathrm{Ca} = 0.2$, and $a = 55$ and $b = 3.5$ for $\mathrm{Ca} = 0.05$. This is explained because, at low capillary numbers, the drop remains nearly spherical and the collision area, which results in coalescence, increases. We observed coalescence for $\mathrm{Ca}_{\mathrm{mag}} > 1$ using $a = 0$ and $b = 0.3$. Also the magnetic field is only applied in y-direction.

4.3.1 Effects on droplet deformation and orientation

The geometry (shape and orientation) of the drops have a major influence on the rheological properties of an emulsion. To quantify how deformed the droplets are under shear and an external magnetic field, we use the Taylor deformation parameter (equation (4.6)). Since we are investigating a system with moderate droplet concentration, the parameter D_T does not exactly describe the shape of the drop because they can deform locally due to the close presence of other drops and also due to the presence of repulsive forces. However, it provides a useful average deformation value to predict the microstructure. Figure 4.6 shows the deformation of each drop over time. The red curve is the average deformation at each instant of all the drops. Note that there are large fluctuations in these values, and one of the reasons is the droplet-droplet hydrodynamic interactions. Sometimes, a drop can pass between two others, undergoing abrupt compression before returning to its equilibrium deformation shape. This process repeats over time. The inset in the plot of Figure 4.6 shows exactly this scenario.

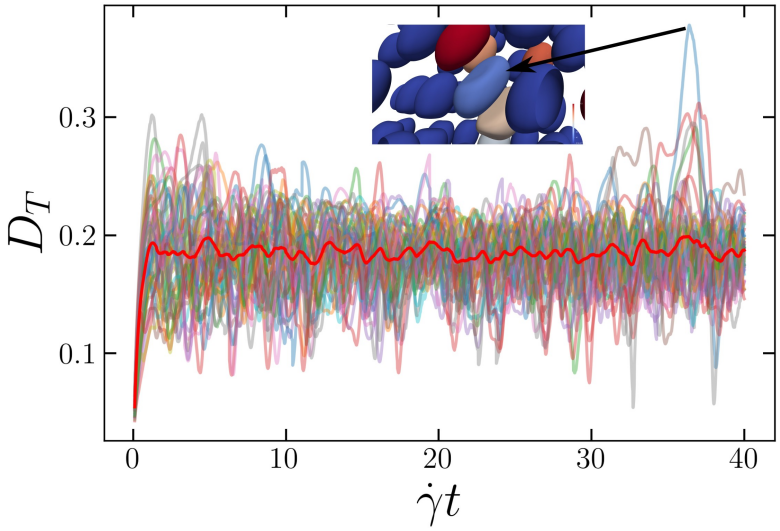

Figure 4.6 – Deformation parameter as a function of time for $\Phi = 0.20$, $\mathrm{Ca} = 0.1$, $\mathrm{Ca_{mag}} = 6$ and $\mathrm{Re} = 0.01$. The red curve represents the average deformation, while the other 48 colored curves represent the deformation of each droplet over time. The insert in the plot shows the droplets from a real simulation at $\dot{\gamma}t = 38$.

Figure 4.7(a) shows the deformation of the ferrofluid emulsion as a function of the magnetic capillary number at a fixed capillary number $\mathrm{Ca} = 0.05$. For low $\mathrm{Ca_{mag}}$, the volume fraction of the droplets has a minor influence on the average deformation. The curves for $\Phi = 0.30$ (blue), $\Phi = 0.20$ (orange), $\Phi = 0.10$ (red), and $\Phi \approx 0$ (black) collapse to a deformation value of around $D_T \approx 0.07$. On the other hand, as $\mathrm{Ca_{mag}}$ increases, the influence of the volume fraction on the deformation of the drops becomes more evident, even for low shear flow (almost spherical drops). Stronger external magnetic fields create a larger magnetic force on the drop interface. This force stretches the drop along the field direction. As a result, deformation increases with increasing magnetic field strength for all droplet concentrations. However, as the volume fraction increases, the drops can be compressed due to surrounding drops. This means that with increasing dispersed-phase volume fraction, both individual and overall deformation decrease. It should be noted that in the absence of a magnetic field, previous research has shown that drops deform more as the dispersed-phase volume fraction is increased Loewenberg and Hinch (1996); we computed this for $\mathrm{Ca_{mag}} = 1$. Figure 4.7(a) and also 4.7(b), which presents $\mathrm{Ca} = 0.05$ and $\mathrm{Ca} = 0.1$, respectively, show this: the emulsion with a single drop reported by Abicalil et al. (2021) exhibits higher average deformation for most magnetic capillary numbers,

except for very small values. Moreover, the curves in these figures display nonmonotonic behavior. Above $\mathrm{Ca_{mag}} = 8$, the deformation tends to plateau, which is more pronounced for higher values of Φ. Figure 4.7(c) shows the results for $Ca = 0.20$, where we computed the breakup of droplets for $\mathrm{Ca_{mag}} \geq 6$. The figure reveals that higher magnetic capillary numbers induce greater droplet deformation. Moreover, we can observe that at $\mathrm{Ca_{mag}} = 4$, higher droplet concentrations lead to less deformation, while the opposite trend is observed for lower magnetic field strengths.

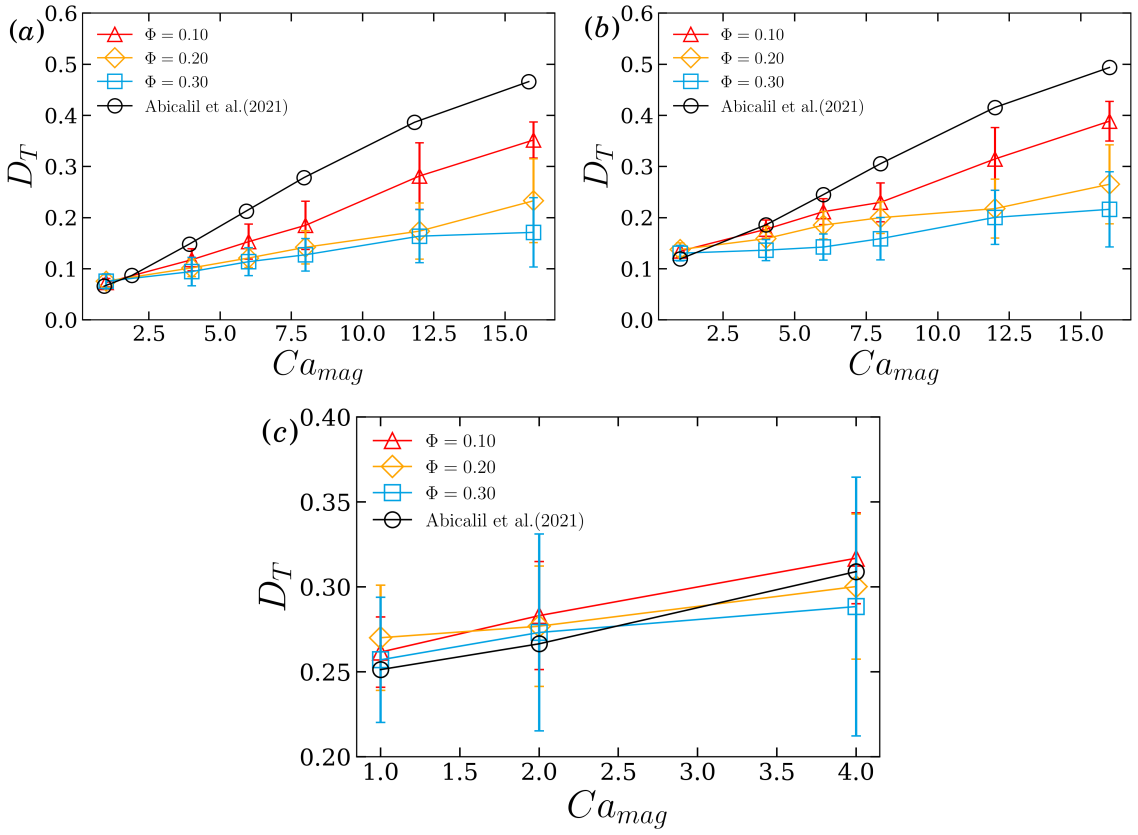

Figure 4.7 – Deformation as a function of magnetic capillary number. The plots are for (a) $Ca = 0.05$, (b) $Ca = 0.1$ and (c) $Ca = 0.2$. We compare our simulation with the diluted case performed by Abicalil et al. (2021). For plots (a) and (b), we set $\mathrm{Ca_{mag}} = 1, 4, 6, 8, 12, 16$. For plot (c), we set $\mathrm{Ca_{mag}} = 1, 2, 4$.

In addition to deforming, both the simple shear and the external magnetic field also tend to orient the drop. Since we are applying a magnetic field in the y-direction, there is a competition between the effects of the imposed flow and the external magnetic field on the geometry of the drops. We compute the angle θ between the semi-major axis ℓ and the x-direction to measure the orientation of the drop. Figure 4.8

presents the inclination angle as a function of time; the hydrodynamic interaction between the droplets contributes to the fluctuations in values over time. Note that $\theta = 90°$ means the droplet is completely aligned in the direction of the external magnetic field applied in the y-direction. Figures 4.9(a) and 4.9(b) show θ as a function of the capillary magnetic number at $\mathrm{Ca} = 0.05$ and $\mathrm{Ca} = 0.10$, respectively. We compared our simulations for $\Phi = 0.10$ and $\Phi = 0.20$ with the diluted case from Abicalil et al. (2021); we did not compute for $\Phi = 0.30$ (just some cases for $\mathrm{Ca} = 0.10$ and $\mathrm{Ca} = 0.2$) due to scarce time since we could measure this parameter. We observe that the average drop orientation decreases as the dispersed-phase volume fraction is increased at a fixed magnetic capillary number. This means that with more surrounding droplets, the magnetic field is less effective in aligning them in its direction, and even for high $\mathrm{Ca}_{\mathrm{mag}}$, this effect is significant. Moreover, for non-magnetic emulsions, Loewenberg and Hinch (1996) also pointed out that the droplets orient more in the flow direction with the increase in volume fraction. However, increasing $\mathrm{Ca}_{\mathrm{mag}}$ leads to the alignment of the drop in the direction of the magnetic field, which increases the average angle until it reaches a plateau for values above $\mathrm{Ca}_{\mathrm{mag}} \approx 8$. Comparing Figures 4.9(a) and 4.9(b), we can notice that the θ values are lower for all simulations with higher shear flow, revealing that the alignment of the drops in the main flow direction is strongly influenced by the shear rate.

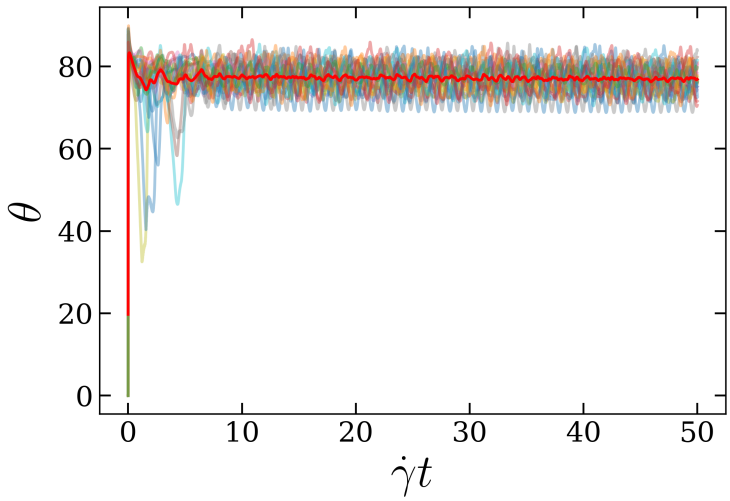

Figure 4.8 – Drop orientation, in degrees, as a function of time for $\Phi = 0.10$, $\mathrm{Ca} = 0.05$, $\mathrm{Ca}_{\mathrm{mag}} = 16$ and $\mathrm{Re} = 0.01$. The red curve represents the average orientation, while the other 24 colored curves represent the inclination of each droplet over time.

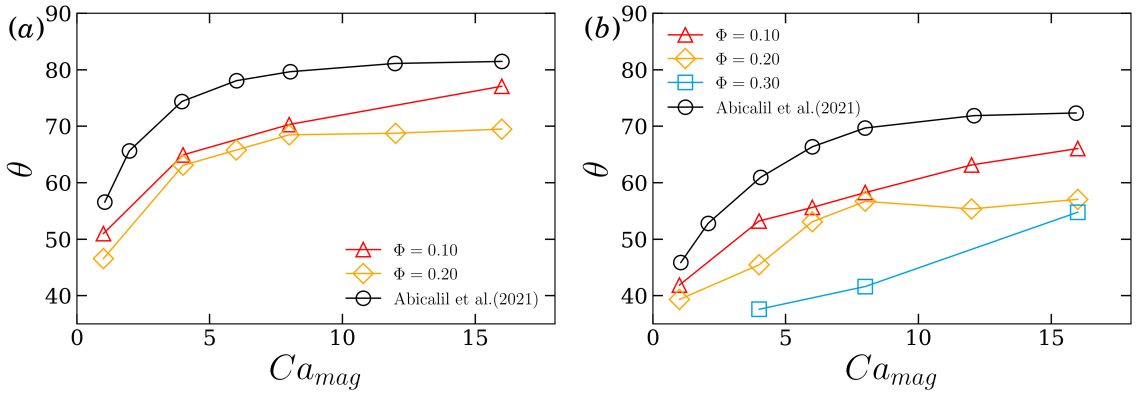

Figure 4.9 – Average droplets orientation, in degrees, as a function of magnetic capillary number. The plots are for (*a*) $Ca = 0.05$ and (*b*) $Ca = 0.1$. We compare our simulation with the diluted case performed by Abicalil et al. (2021).

4.3.2 Effects on shear viscosity

As seen in the previous section, when the droplets in an emulsion are under shear, they tend to deform and align in the flow direction, resulting in shear thinning behavior. On the other hand, when an external magnetic field is applied, the magnetic droplets also respond to this field. The competition between these two effects, changes the geometry of the droplet, which consequently changes the viscosity of the emulsion. From Figure 4.10, panels (a) and (b) correspond to simulations with Ca = 0.05, (c) and (d) to Ca = 0.1, and (e) and (f) to Ca = 0.20. Figures 4.10(a), (c), and (e) show the effective viscosity as a function of volume fraction for different magnetic capillary numbers. Overall, we observe in all these three panels that the shear viscosity increases as the volume fraction increases. Moreover, at a fixed Φ, as the magnetic capillary number is increased, the droplets tend to align themselves in the direction of the applied external magnetic field, resulting in higher effective viscosity. In weak flow (panel a), this effect is more pronounced than in those with higher shear rates (panels c and e). For $Ca_{mag} = 12$ and $Ca_{mag} = 6$ in panels (a) and (c), the curves do not exhibit a monotonic behavior, indicating that in more concentrated emulsions, this value may reaches a constant viscosity. Figures 4.10(b), (d), and (f) show the reduced viscosity as a function of magnetic capillary numbers. In these three graphs, we observed that with an increase in the number of droplets, the reduced viscosity increases. On the other hand, plot (f) is for Ca = 0.2 and in this case, the effect of shear seems to surpass the magnetic effect such that the droplet becomes more de-

formed in the x direction than in the direction of the external magnetic field. For $\mathrm{Ca_{mag}} = 4$ and $\Phi = 0.30$ in plot (f), the reduced viscosity is approximately $\eta_{red} \approx 0.65$. In comparison, for plot (b), the reduced viscosity is $\eta_{red} \approx 1.2$ for the same case.

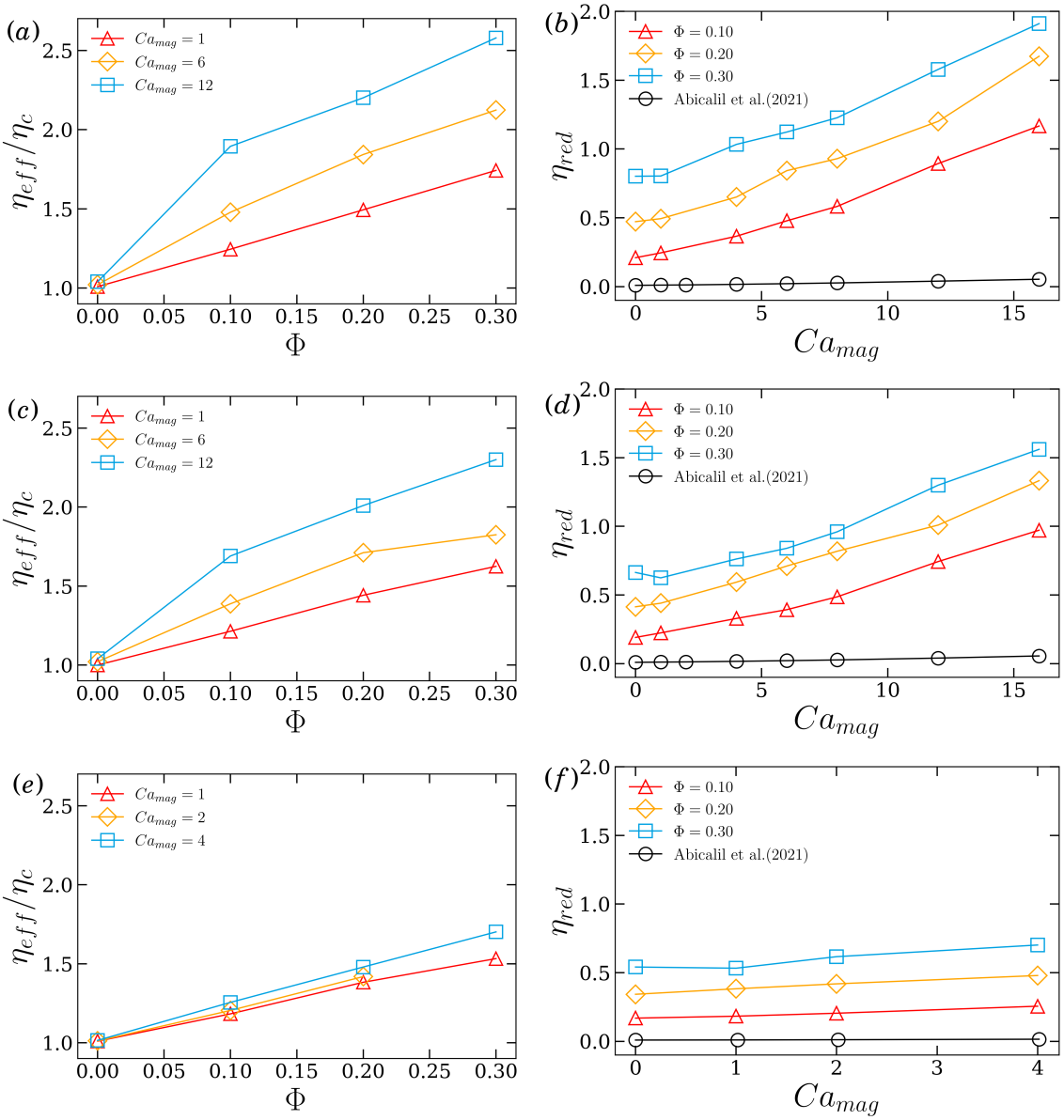

Figure 4.10 – Effective viscosity as a function of ferrofluid droplets concentrations (left column). Reduced viscosity as a function of magnetic capillary number. Three capillary numbers were considered, increasing from top to bottom. The portion (a-b) $\mathrm{Ca} = 0.05$; (c-d) $\mathrm{Ca} = 0.10$; (e-f) $\mathrm{Ca} = 0.2$.

The contribution of each droplet to viscosity becomes more prominent when we normalize this property by the volume fraction. Figure 4.11 shows the reduced viscosity per volume fraction as a function of magnetic capillary number. We observe that as the shear rate increases, droplets in the diluted regime contribute more to viscosity. This occurs because droplets can deform more freely in diluted systems compared to those with higher volume fractions when under the action of magnetic fields at moderate to high $\mathrm{Ca_{mag}}$ (see Figure 4.7). Note that, at a low shear rate η_{red}/Φ as a function of $\mathrm{Ca_{mag}}$ is higher for $\Phi = 0.10$ than for the dilute case. This suggests the formation of structures due to magnetic interactions between droplets, as the weak flow is not strong enough to break them apart. In plot (b), for strong magnetic field (high $\mathrm{Ca_{mag}}$), the viscosity difference between the concentrated ($\Phi = 0.10$) and dilute cases becomes less significant. Here, the stronger flow starts to influence the behavior of the droplets, leading to more prominent breakage of these structures.

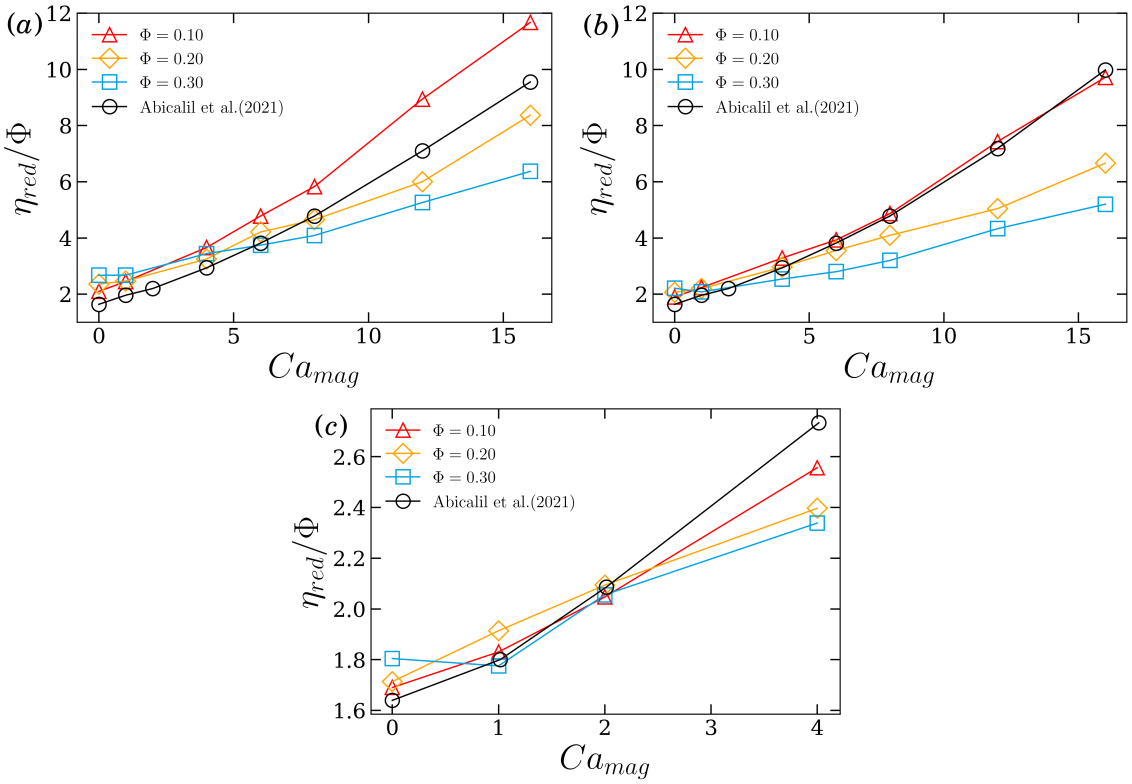

Figure 4.11 – Reduced viscosity normalized by Φ as a function of magnetic capillary number for $\mathrm{Ca} = 0.05(a)$, $\mathrm{Ca} = 0.10(b)$ and $\mathrm{Ca} = 0.20(c)$.

4.3.3 Effects on magnetization

The magnetization is determined by equation (2.24). Although each ferrofluid droplet becomes magnetized when an external magnetic field is applied, we measure the bulk magnetization of the emulsion $\langle \mathbf{M} \rangle$. The left column of Figure 4.12 shows the magnetization scaled by the external magnetic field intensity H_0 as a function of magnetic capillary number, while the right column shows the same parameters but the magnetization is normalized by the volume fraction of droplets. Panels (a) and (b) correspond to simulations with $\mathrm{Ca} = 0.05$, (c) and (d) to $\mathrm{Ca} = 0.1$, and (e) and (f) to $\mathrm{Ca} = 0.20$. For the plots in the left column, the bulk magnetization increases with the volume fraction in all cases, but initially shows no significant variation with increasing external magnetic field strength. However, when we normalize $\langle \mathbf{M} \rangle$ by Φ, the contribution of each droplet becomes evident. As $\mathrm{Ca}_{\mathrm{mag}}$ increases, the droplets deform more, as explained in the previous section. The deformation of the droplets is closely related to magnetization, as discussed by Cunha et al. (2020). From panels (b), (d), and (f), as the shear flow increases, the magnetization decreases for all volume fractions. This occurs because shear stress tends to align the droplets in the main flow direction, thus the droplets are less stretched by the magnetic field, resulting in lower magnetization. Also, Figures 4.13(a), (c), and (e) show the magnetization as a function of ferrofluid droplet concentration normalized by Φ. Comparing the curves for $\mathrm{Ca}_{\mathrm{mag}} = 1$, $\mathrm{Ca}_{\mathrm{mag}} = 6$, and $\mathrm{Ca}_{\mathrm{mag}} = 12$ at different Ca, we observe that the droplet contribution to the bulk magnetization decreases as the shear increases. Moreover, as Φ increases, magnetization decreases non-monotonically because the droplets deform less due to the presence of neighboring drops that activate repulsive forces, resulting in compression of the drops. Panels (b), (d), and (f) show the magnetization as a function of volume fraction. For all $\mathrm{Ca}_{\mathrm{mag}}$ curves, magnetization increases almost linearly with the volume fraction of droplets.

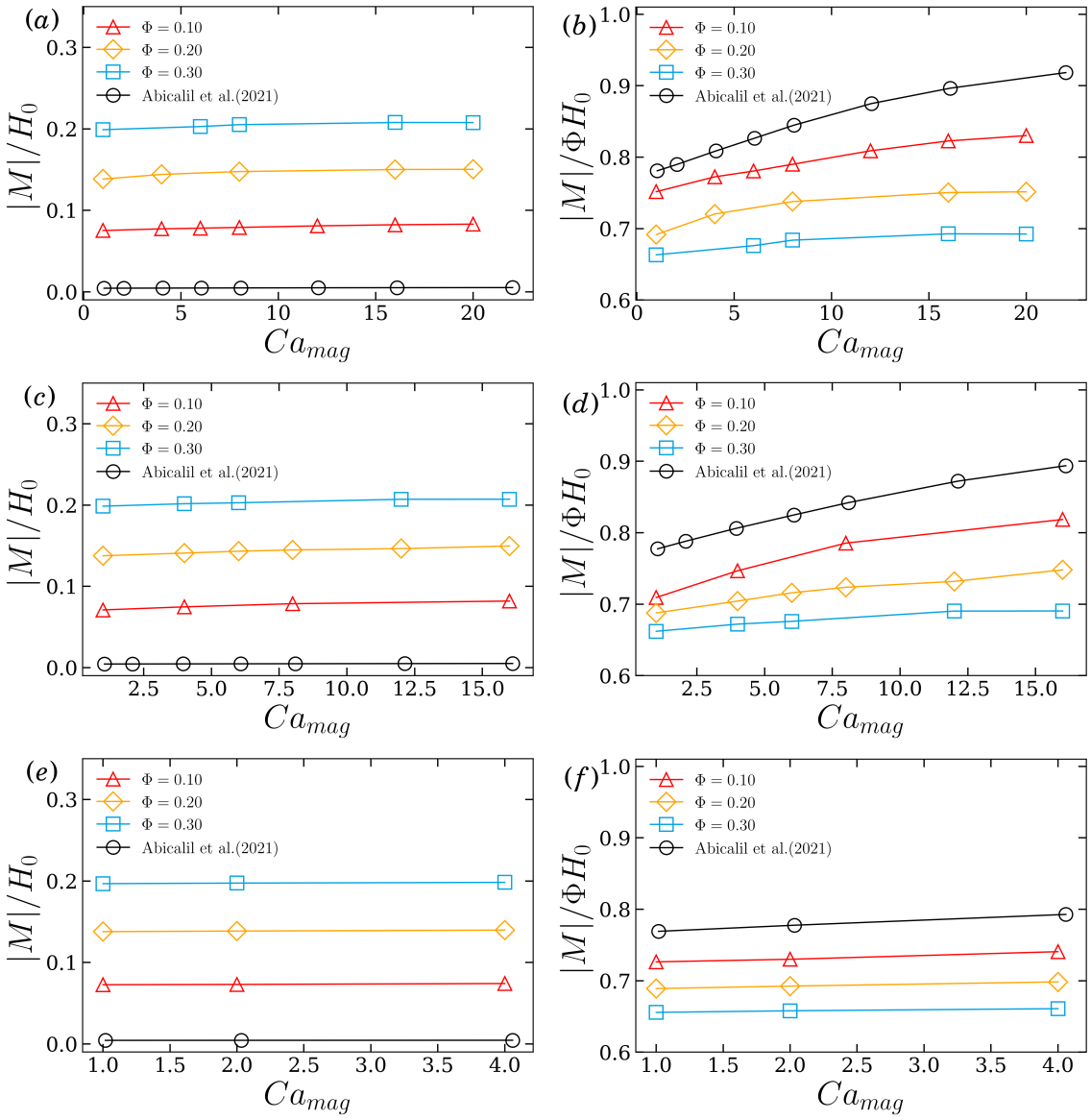

Figure 4.12 – Mean emulsion magnetization as a function of magnetic capillary number (left column). Mean emulsion magnetization as a function of magnetic capillary number normalized by Φ (right column). Three capillary numbers were considered, increasing from top to bottom: (a-b) Ca = 0.05; (c-d) Ca = 0.10; (e-f) Ca = 0.20. We compare our simulations with diluted cases reported by Abicalil et al. (2021)..

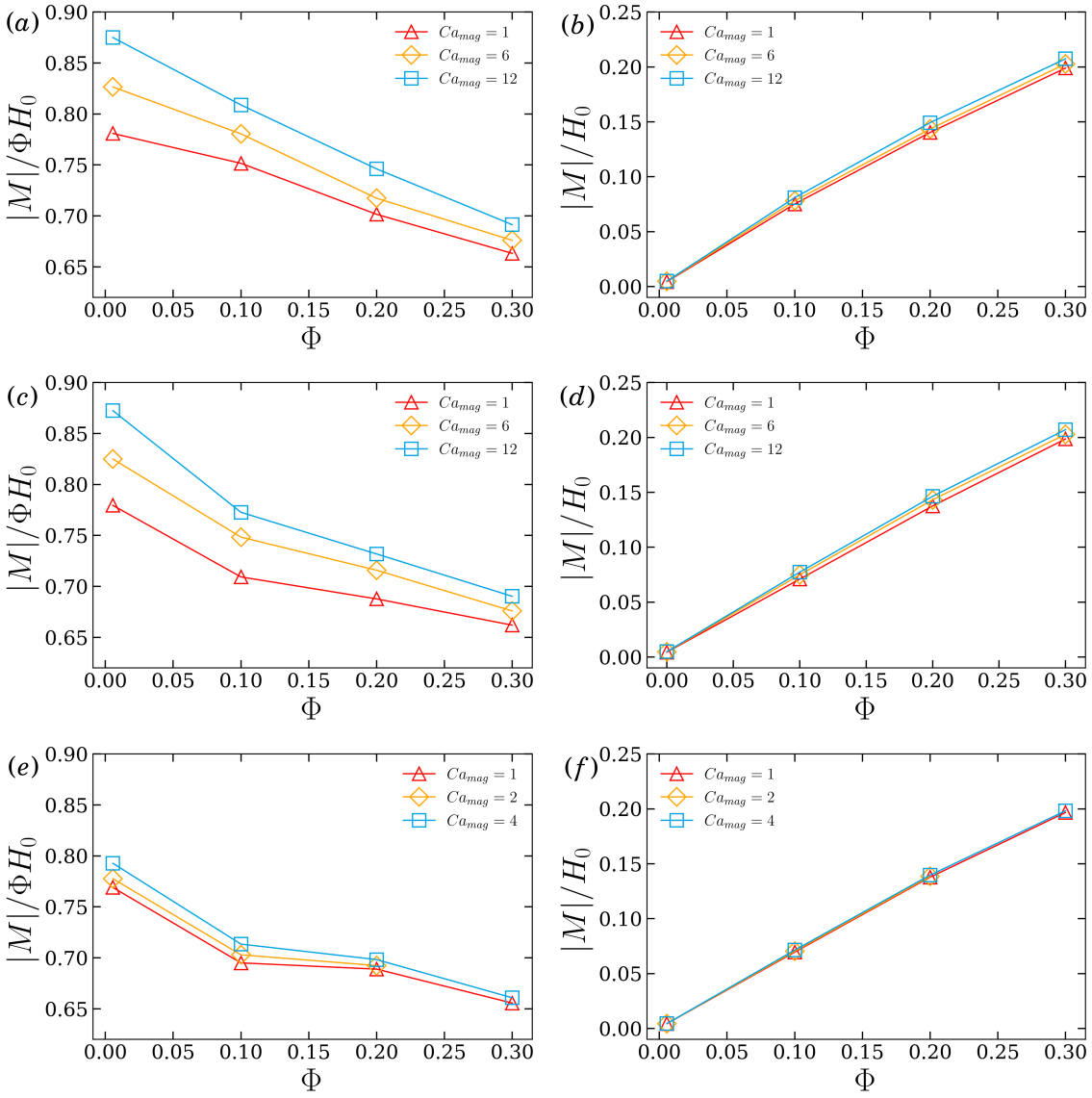

Figure 4.13 – Mean emulsion magnetization as a function of droplet volume fraction normalized by Φ (left column). Mean emulsion as a function of droplet volume fraction (right column). Three capillary numbers were considered, increasing from top to bottom: (a-b) Ca = 0.05; (c-d) Ca = 0.10; (e-f) Ca = 0.20.

4.3.4 Effects on magnetic angle

While we assume the droplets are superparamagnetic, a slight misalignment angle between $\langle \mathbf{M} \rangle$ and $\mathbf{H}_0$ is observed (see Figure 4.14). The right-hand plot of Figure 4.15 shows the time evolution of θ_{mag}, revealing a quasi-periodic behavior. In magnetic emulsions at moderate concentrations, droplets can form chains under an

external magnetic field, similar to what occurs in ferrofluids. On the other hand, under shear flow, the emulsion experiences diffusive motion due to shear-induced hydrodynamic interactions between the droplets (Malipeddi and Sarkar, 2019), which induces drop dispersion. When the ferrofluid emulsion is subjected to both shear and magnetic field, the droplets tend to align with the external magnetic field, while the shear tends to orient them in the main flow direction, leading to a dispersive process. This competition on average results in fluctuations of θ_{mag} over time, as shown in Figure 4.15a. The Fourier transform of this signal indicates the presence of dominant frequencies in the system, which could be associated with the breaking and formation of chains.

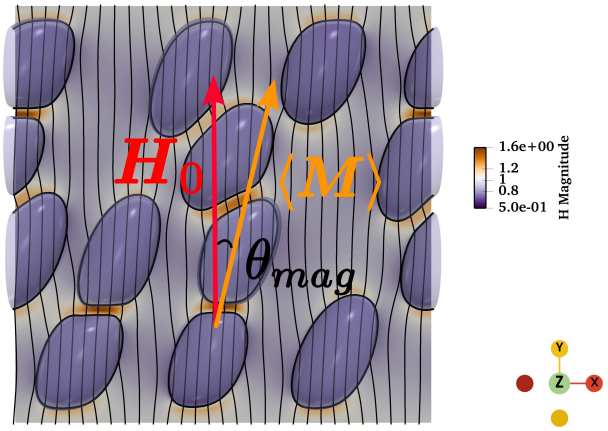

Figure 4.14 – Snapshots of the emulsion simulation under an applied magnetic field applied in y direction.

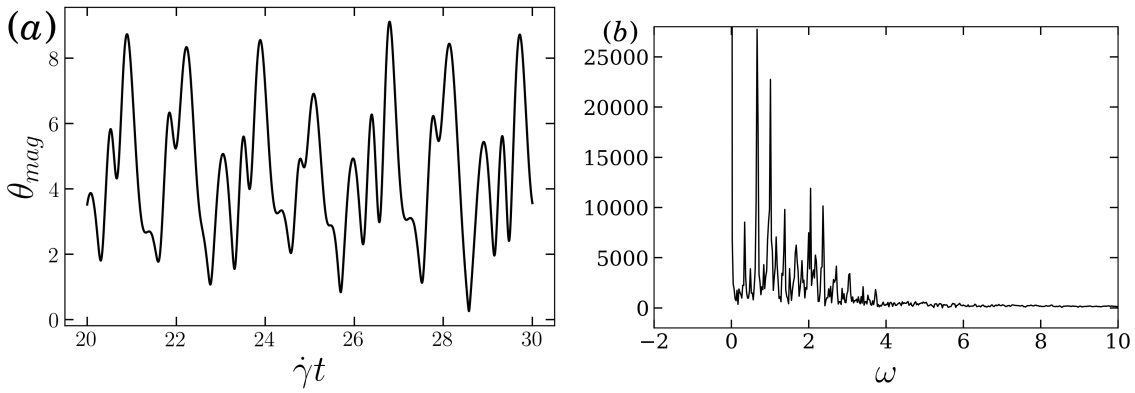

Figure 4.15 – (a) Angle between the ferrofluid emulsion bulk magnetization and the external field directio, in degrees, over time for $\Phi = 0.30$, $\mathrm{Ca} = 0.10$ and $\mathrm{Ca_{mag}} = 6$ (left plot). (b) Signal of θ_{mag} decomposed into its frequency ω components using fast fourier transform (right plot).

Figure 4.16 shows the misalignment angle between the bulk magnetization and the external magnetic field for two magnetic capillary numbers. In the left plot, the magnetic capillary number is $\mathrm{Ca_{mag}} = 1$, while in the right plot it is $\mathrm{Ca_{mag}} = 16$. Comparing both, we observe that the increase in the external magnetic field can dominate the droplet orientation at a fixed capillary number. Thus, the quasi-periodic behavior of θ_{mag} is less pronounced at high $\mathrm{Ca_{mag}}$. For this case, the formation of chains or layers is more probable. Moreover, Figure 4.17 shows two plots for the misalignment angle θ_{mag} as a function of the magnetic capillary number. From the results for $\mathrm{Ca} = 0.05$ (left plot), the ferrofluid emulsion with $\Phi = 0.10$ has a higher misalignment angle value than for higher concentrations at most $\mathrm{Ca_{mag}}$ values. It can be concluded that the increase in volume fraction hinders the alignment and misalignment of each droplet. A similar behavior is also observed for misalignment angle between the bulk magnetization and the external magnetic field for $\mathrm{Ca} = 0.1$ (right plot).

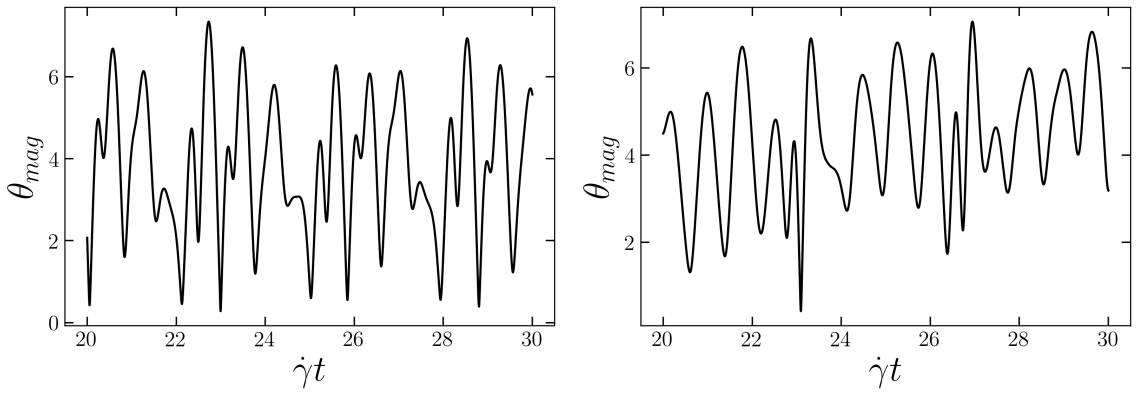

Figure 4.16 – Angle between the ferrofluid emulsion bulk magnetization and the external field direction, in degrees, over time for $\Phi = 0.30$, $\mathrm{Ca} = 0.10$, $\mathrm{Ca_{mag}} = 1$ (left plot) and $\mathrm{Ca_{mag}} = 16$ (right plot).

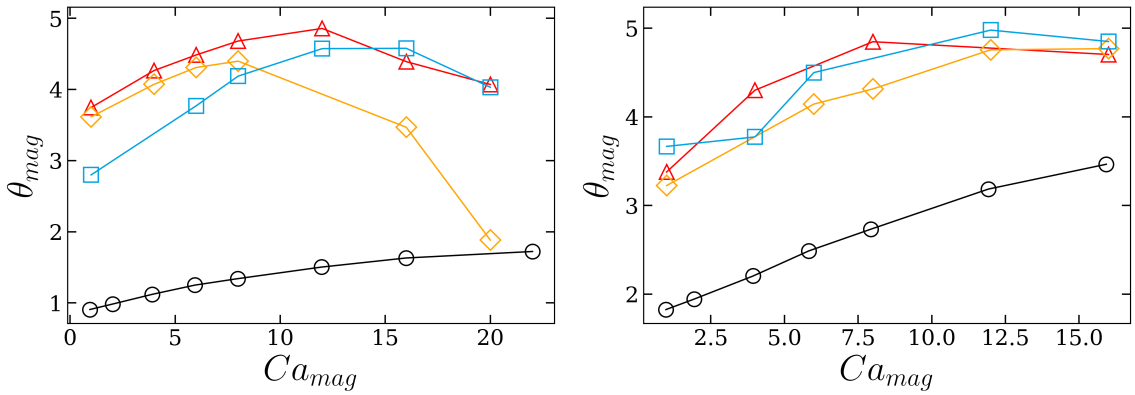

Figure 4.17 – Misalignment angle between the ferrofluid emulsion bulk magnetization and the external field direction, in degrees, as a function of magnetic capillary number for $\mathrm{Ca} = 0.05$ (left plot) and $\mathrm{Ca} = 0.1$ (right plot). The red curves with triangle symbols correspond to $\Phi = 0.10$, the orange curves with diamond symbols correspond to $\Phi = 0.20$, the blue curves with square symbols correspond to $\Phi = 0.30$, and the black curve with circle symbols represents the diluted case performed by Abicalil et al. (2021).

The misalignment between the applied magnetic field and the magnetization creates a torque on each droplet. This magnetic torque, from a macroscopic point of view, can be defined as

$$\boldsymbol{\tau}_{\mathrm{mag}} = \frac{\mathrm{Ca}_{\mathrm{mag}}}{\mathrm{Ca}} \langle \mathbf{M} \rangle \times \mathbf{H}_0, \tag{4.2}$$

where its intensity is given by $\tau_{mag} = (\mathrm{Ca}_{\mathrm{mag}}/\mathrm{Ca})|\mathbf{M}|\sin(\theta_{mag})$. In the absence of an external magnetic field, the angular momentum balance equation leads to the sum of external torques being equal to zero, hence the hydrodynamic torque is zero. This means that the drops are torque-free and rotate with the vorticity of the shear flow. However, with an external magnetic field, there is a magnetic torque acting on the drops. This results in a balance where the magnetic torque is equal to the negative of the hydrodynamic torque. Figure 4.18(a) shows the magnetic torque as a function of the magnetic capillary number. This result reveals that τ_{mag} increases when Φ increases. Note that the torque values are always positive, thus there is a counterclockwise rotation which agrees with the work of Abicalil (2021). On the other hand, in Figure 4.18(b), the magnetic torque for $\Phi = 0.10$ is greater than that for $\Phi = 0.30$. One explanation is that at lower concentrations, a drop has fewer neighboring drops, allowing it to rotate more. For $\Phi = 0.30$ there are many drops close to each other, making it difficult for each to rotate, and the bulk torque decreases. Also, τ_{mag}

has a monotonic behavior with the magnetic capillary number.

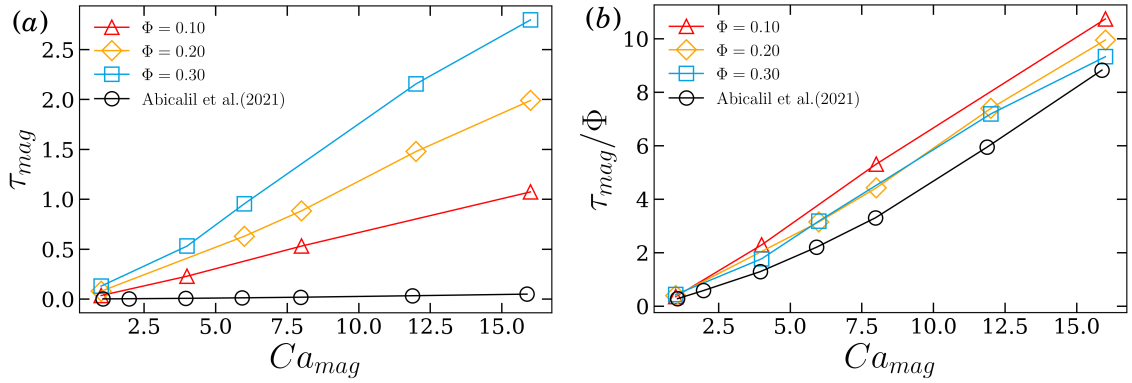

Figure 4.18 – (*a*) Magnetic torque as a function of magnetic capillary number for $\mathrm{Ca} = 0.1$ and $\mathrm{Re} = 0.01$. (*b*) Magnetic torque normalized by volume fraction as a function of magnetic capillary number for $\mathrm{Ca} = 0.1$ and $\mathrm{Re} = 0.01$.

5 Conclusion and future work

The main goal of this work was to get a better understanding of non-dilute ferrofluid emulsions subjected to simple shear flow and an external magnetic field applied solely in the direction of the main velocity gradient (y-direction). We investigated the combined effects of these two mechanisms, which disrupt the equilibrium of the emulsion, on bulk properties, including average droplet deformation, effective viscosity, magnetization, magnetic misalignment angle, and magnetic torque. Moreover, we evaluated the effect of the droplet volume fraction on these properties. Our analysis was performed using a three-dimensional numerical domain where monodispersed ferrofluid droplets are randomly distributed in a non-magnetic fluid. Both phases have the same density and viscosity, where inertial effects are not significant. The domain was discretized using the finite-difference method, the level set method was employed to capture the interface, and the second-order projection method was used to solve the Navier-Stokes equations. We implemented a repulsive force between droplets to completely prevent them from merging (coalescence). To ensure this force is effective, we tested different calibration coefficients. These coefficients control the strength of the repulsion between the droplets. We found that under weak flow conditions, where the restoring mechanism of the droplet is strong, a larger collision surface is noted. Consequently, coefficients similar to those used in previous studies were employed. However, as the droplets became more elongated with increasing shear rates, it is possible to decrease the intensity of the repulsive force. It is important to note that this collision model does not represent a direct physical phenomenon. Instead, it serves as an artificial implementation solely designed to prevent droplet coalescence, given the limitations of achieving a highly refined mesh. This is also why we could not reproduce the experimental results of the vertical displacement in pairwise interactions between droplets.

As a result, we first simulated cases considering a non-magnetic emulsion with an imposed simple shear. We observed that the effective viscosity does not have a linear behavior with increasing droplet concentration. Once the interactions between droplets become significant, the problem becomes highly non-linear, revealing a dynamic response. In addition, we determined the effective viscosity for different shear rates and observed shear-thinning behavior. We also computed a droplet breakup

case for $\Phi = 0.30$ at $Ca = 0.30$, which was not predicted in previous works using different numerical methodologies. Overall, our results for the viscosity of non-magnetic droplets agree well with previous studies, ensuring that the repulsive force between the droplets is effective and that our numerical methods are well-implemented.

While the existing literature has mainly focused on examining single-droplet ferrofluid emulsions, we investigated a system with multiple ferrofluid droplets. Our findings reveal that at a fixed shear rate, the average deformation of the emulsion increases with stronger magnetic field strength while decreasing with the rise in droplet concentration. This observation can be attributed to two primary factors. First, as the magnetic field intensity increases, the droplets exhibit a tendency to align along the direction of the field. This alignment promotes a more elongated droplet shape, contributing to the observed increase in deformation and inclination. On the other hand, as the droplet concentration increases, the proximity between them limits their ability to deform and align effectively in response to the magnetic field. This constraint results in a decrease in the average deformation of the emulsion. Also, with increased shear rates, the droplets align more with the flow direction and deform more. The geometry of the droplet directly influences the macroscopic response of the emulsion. Therefore, the effective viscosity increases with higher magnetic field strength due to greater deformation and alignment in the direction of the applied external field. An increase in viscosity is also observed with higher volumetric fraction. In contrast, when the viscosity is normalized by Φ, it is revealed that the contribution of a droplet in a dilute regime is greater than that in a semi-dilute regime. Along with the observed deformation changes, we also found that as the droplets become more elongated under the influence of the increasing magnetic field, their bulk magnetization also increases. This correlation arises because droplet shape directly influences magnetization. Our investigations revealed a monotonic behavior of magnetization with respect to the volume fraction. When normalized, we observed that droplets in the diluted regime exhibit a higher average magnetization compared to those in a concentrated system. Furthermore, we determined that the misalignment angle between the external magnetic field and the magnetization increases for a non-diluted emulsion. This increase is directly associated with the presence and enhancement of the magnetic torque, which acts to rotate the droplet into alignment with the external field.

Although this study provides some contributions to understanding the behavior of non-dilute ferrofluid emulsions, it is still in its early stages and many questions remain unanswered. Here are some ideas for future research:

- Include the contribution of the repulsive force in the stresslet and thereby study the complete rheology of the system;
- Obtain probability distribution functions as well as pair distribution functions for a better understanding of the dynamics of the magnetic emulsion under shear and external magnetic field;
- Reduce the droplet size to increase the number of droplets for the same droplet volume fractions as in this study. A larger number of particles contributes to more statistically significant results;
- Considering a polydisperse system to represent a ferrofluid emulsion more realistically;
- Analyze the influence of initial conditions on the system's response;
- Investigate the impact of confinement on the system's behavior;
- Employ small amplitude oscillatory shear (SAOS) instead of simple shear, and also an external magnetic field. Identifying a characteristic frequency of the system enables a more in-depth dynamic analysis;
- Investigate strategies to achieve higher droplet volume fractions in ferrofluid emulsions. In addition, explore the potential of an applied magnetic field to modulate the yield stress of highly concentrated ferrofluid emulsions;
- Investigate how different viscosity ratios influence the microstructure and properties of the non-dilute emulsion;
- Investigate the influence of the external magnetic field on droplet breakup in the non-dilute regime.

5 Bibliography

Abdo, R. F., Abicalil, V. G., Cunha, L. H., and Oliveira, T. F. (2023). On the rheology and magnetization of dilute magnetic emulsions under small amplitude oscillatory shear. *Journal of Fluid Mechanics*, 955:A3. (Cited on pages 7 and 21.)

Abicalil, V. G. (2021). Rheology and magnetization of dilute ferrofluid emulsions. (Cited on pages 7, 18, 19, 34, and 54.)

Abicalil, V. G., Abdo, R. F., da Cunha, L. H. P., de Oliveira, T. F., et al. (2021). On the magnetization of dilute ferrofluid emulsions in shear flows. *Physics of Fluids*, 33(5). (Cited on pages v, vi, 4, 7, 43, 44, 45, 46, 50, and 54.)

Afkhami, S. a., Tyler, A., Renardy, Y., Renardy, M., Pierre, T. S., Woodward, R., and Riffle, J. S. (2010). Deformation of a hydrophobic ferrofluid droplet suspended in a viscous medium under uniform magnetic fields. *Journal of Fluid Mechanics*, 663:358–384. (Cited on pages iii, 3, 4, and 7.)

Amani, A., Balcázar, N., Castro, J., and Oliva, A. (2019). Numerical study of droplet deformation in shear flow using a conservative level-set method. *Chemical Engineering Science*, 207:153–171. (Cited on pages 6 and 18.)

Aris, R. (2012). *Vectors, tensors and the basic equations of fluid mechanics*. Courier Corporation. (Cited on page 11.)

Bashir, S., Rees, J. M., and Zimmerman, W. B. (2011). Simulations of microfluidic droplet formation using the two-phase level set method. *Chemical Engineering Science*, 66(20):4733–4741. (Cited on page 18.)

Batchelor, G. (1970). The stress system in a suspension of force-free particles. *Journal of fluid mechanics*, 41(3):545–570. (Cited on page 6.)

Batchelor, G. (1972). The determination of the bulk stress in a suspension of spherical particles to order c2. *Journal of Fluid Mechanics*, 56(3):401–427. (Cited on page 5.)

Bibette, J. (1993). Monodisperse ferrofluid emulsions. *Journal of magnetism and magnetic materials*, 122(1-3):37–41. (Cited on pages 1 and 7.)

Brady, J. F. and Bossis, G. (1985). The rheology of concentrated suspensions of spheres in simple shear flow by numerical simulation. *Journal of Fluid mechanics*, 155:105–129. (Cited on page 5.)

Capobianchi, P., Lappa, M., and Oliveira, M. S. (2018). Deformation of a ferrofluid droplet in a simple shear flow under the effect of a constant magnetic field. *Computers & Fluids*, 173:313–323. (Cited on page 7.)

Capobianchi, P., Lappa, M., Oliveira, M. S., and Pinho, F. T. (2021). Shear rheology of a dilute emulsion of ferrofluid droplets dispersed in a nonmagnetizable carrier fluid under the influence of a uniform magnetic field. *Journal of Rheology*, 65(5):925–941. (Cited on page 7.)

Cunha, L., Siqueira, I., Cunha, F., and Oliveira, T. (2020). Effects of external magnetic fields on the rheology and magnetization of dilute emulsions of ferrofluid droplets in shear flows. *Physics of Fluids*, 32(7). (Cited on pages 4, 7, and 49.)

Cunha, L. H., Siqueira, I. R., Oliveira, T. F., and Ceniceros, H. D. (2018). Field-induced control of ferrofluid emulsion rheology and droplet break-up in shear flows. *Physics of Fluids*, 30(12). (Cited on pages 7 and 18.)

De Vita, F., Rosti, M. E., Caserta, S., and Brandt, L. (2019). On the effect of coalescence on the rheology of emulsions. *Journal of Fluid Mechanics*, 880:969–991. (Cited on pages iv, 7, 26, 29, 30, and 33.)

Derkach, S. (2010). Rheology on the way from dilute to concentrated emulsions. *International Review of Chemical Engineering*, 2(3):465–472. (Cited on page 7.)

Einstein, A. (1906). A new determination of molecular dimensions. *Annln., Phys.*, 19:289–306. (Cited on page 5.)

Einstein, A. (1911). Berichtigung zu meiner arbeit: Eine neue bestimmung der moleküldimensionen. *Annalen der Physik*, 339(3):591–592. (Cited on page 5.)

Fan, X., Jiang, Y., Li, M., Zhang, Y., Tian, C., Mao, L., Xie, H., Sun, L., Yang, Z., and Sitti, M. (2022). Scale-reconfigurable miniature ferrofluidic robots for negotiating sharply variable spaces. *Science Advances*, 8(37):eabq1677. (Cited on pages iii and 2.)

Fan, X., Sun, M., Sun, L., and Xie, H. (2020). Ferrofluid droplets as liquid microrobots with multiple deformabilities. *Advanced Functional Materials*, 30(24):2000138. (Cited on page 2.)

Faroughi, S. A. and Huber, C. (2015). A generalized equation for rheology of emulsions and suspensions of deformable particles subjected to simple shear at low reynolds number. *Rheologica Acta*, 54:85–108. (Cited on page 6.)

Griffiths, D. J. (2023). *Introduction to electrodynamics*. Cambridge University Press. (Cited on page 11.)

Guido, S. (2011). Shear-induced droplet deformation: Effects of confined geometry and viscoelasticity. *Current opinion in colloid & interface science*, 16(1):61–70. (Cited on page 6.)

Guido, S. and Simeone, M. (1998). Binary collision of drops in simple shear flow by computer-assisted video optical microscopy. *Journal of Fluid Mechanics*, 357:1–20. (Cited on pages iv, 30, and 31.)

Guido, S. and Villone, M. (1998). Three-dimensional shape of a drop under simple shear flow. *Journal of rheology*, 42(2):395–415. (Cited on page 6.)

Guilherme, A., Siqueira, I., Cunha, L., Thompson, R., and Oliveira, T. (2023). Ferrofluid droplets in planar extensional flows: Droplet shape and magnetization reveal novel rheological signatures of ferrofluid emulsions. *Physical Review Fluids*, 8(6):063601. (Cited on pages 4 and 13.)

Hassan, M. R. and Wang, C. (2020). Ferro-hydrodynamic interactions between ferrofluid droplet pairs in simple shear flows. *Colloids and Surfaces A: Physicochemical and Engineering Aspects*, 602:124906. (Cited on page 7.)

Hassan, M. R., Zhang, J., and Wang, C. (2018). Deformation of a ferrofluid droplet in simple shear flows under uniform magnetic fields. *Physics of Fluids*, 30(9). (Cited on page 7.)

Ioannou, N., Liu, H., and Zhang, Y. (2016). Droplet dynamics in confinement. *Journal of Computational Science*, 17:463–474. (Cited on page 6.)

Ishida, S. and Matsunaga, D. (2020). Rheology of a dilute ferrofluid droplet suspension in shear flow: Viscosity and normal stress differences. *Physical Review Fluids*, 5(12):123603. (Cited on page 7.)

Jansen, K., Agterof, W., and Mellema, J. (2001). Droplet breakup in concentrated emulsions. *Journal of rheology*, 45(1):227–236. (Cited on page 6.)

Jesus, W. C., Roma, A. M., and Ceniceros, H. D. (2018). Deformation of a sheared magnetic droplet in a viscous fluid. *Commun. Comput. Phys*, 24(2):332–355. (Cited on page 7.)

Kawabata, Y., Ishida, S., and Imai, Y. (2024). Deformation and breakup of a ferrofluid droplet in shear flow under magnetic field. *Physics of Fluids*, 36(3). (Cited on page 7.)

Kennedy, M. R., Pozrikidis, C., and Skalak, R. (1994). Motion and deformation of liquid drops, and the rheology of dilute emulsions in simple shear flow. *Computers & fluids*, 23(2):251–278. (Cited on page 6.)

Kim, J. and Moin, P. (1985). Application of a fractional-step method to incompressible navier-stokes equations. *Journal of computational physics*, 59(2):308–323. (Cited on page 22.)

Kondaraju, S., Farhat, H., and Lee, J. S. (2012). Study of aggregational characteristics of emulsions on their rheological properties using the lattice boltzmann approach. *Soft Matter*, 8(5):1374–1384. (Cited on page 7.)

Kwak, S. and Pozrikidis, C. (1998). Adaptive triangulation of evolving, closed, or open surfaces by the advancing-front method. *Journal of Computational Physics*, 145(1):61–88. (Cited on page 6.)

Larson, R. G. and Wei, Y. (2019). A review of thixotropy and its rheological modeling. *Journal of Rheology*, 63(3):477–501. (Cited on page 4.)

Loewenberg, M. (1998). Numerical simulation of concentrated emulsion flows. (Cited on pages v, 6, 38, 39, and 41.)

Loewenberg, M. and Hinch, E. (1996). Numerical simulation of a concentrated emulsion in shear flow. *Journal of Fluid Mechanics*, 321:395–419. (Cited on pages 6, 39, 43, and 45.)

Loewenberg, M. and Hinch, E. (1997). Collision of two deformable drops in shear flow. *Journal of Fluid Mechanics*, 338:299–315. (Cited on page 31.)

Malipeddi, A. R. and Sarkar, K. (2019). Collective diffusivity in a sheared viscous emulsion: Effects of viscosity ratio. *Physical Review Fluids*, 4(9):093603. (Cited on page 52.)

Mason, T., Bibette, J., and Weitz, D. (1996). Yielding and flow of monodisperse emulsions. *Journal of colloid and interface science*, 179(2):439–448. (Cited on page 7.)

Mason, T. G. (1999). New fundamental concepts in emulsion rheology. *Current Opinion in Colloid & Interface Science*, 4(3):231–238. (Cited on pages iii and 4.)

McAdams, A., Sifakis, E., and Teran, J. (2010). A parallel multigrid poisson solver for fluids simulation on large grids. In *Symposium on Computer Animation*, volume 65, page 74. (Cited on page 34.)

Montagne, F., Mondain-Monval, O., Pichot, C., Mozzanega, H., and Elaıssari, A. (2002). Preparation and characterization of narrow sized (o/w) magnetic emulsion. *Journal of magnetism and magnetic materials*, 250:302–312. (Cited on pages iii, 1, 2, and 3.)

Moore, C. C. (2015). Ergodic theorem, ergodic theory, and statistical mechanics. *Proceedings of the National Academy of Sciences*, 112(7):1907–1911. (Cited on page 36.)

Osher, S. and Fedkiw, R. (2006). *Level set methods and dynamic implicit surfaces*, volume 153. Springer Science & Business Media. (Cited on pages 19, 21, and 24.)

Osher, S. and Sethian, J. A. (1988). Fronts propagating with curvature-dependent speed: Algorithms based on Hamilton-Jacobi formulations. *Journal of Computational Physics*, 79(1):12–49. (Cited on page 18.)

Otsubo, Y. and Prud'homme, R. K. (1994). Rheology of oil-in-water emulsions. *Rheologica acta*, 33:29–37. (Cited on page 4.)

Pal, R. (2001). Novel viscosity equations for emulsions of two immiscible liquids. *Journal of Rheology*, 45(2):509–520. (Cited on pages v, 6, 15, 38, and 39.)

Peng, D., Merriman, B., Osher, S., Zhao, H., and Kang, M. (1999). A pde-based fast local level set method. *Journal of computational physics*, 155(2):410–438. (Cited on pages 20 and 24.)

Pimenta, P. H. N. and Oliveira, T. F. d. (2021). Study on the rheology of a dilute emulsion of surfactant-covered droplets using the level set and closest point methods. *Physics of Fluids*, 33(10). (Cited on pages 18 and 33.)

Rallison, J. (1984). The deformation of small viscous drops and bubbles in shear flows. *Annual review of fluid mechanics*, 16(1):45–66. (Cited on page 6.)

Rosensweig, R. (2013). *Ferrohydrodynamics*. Dover Books on Physics. Dover Publications. (Cited on page 13.)

Rosti, M. E., De Vita, F., and Brandt, L. (2019). Numerical simulations of emulsions in shear flows. *Acta Mechanica*, 230(2):667–682. (Cited on page 7.)

Shardt, O., Derksen, J., and Mitra, S. K. (2013). Simulations of droplet coalescence in simple shear flow. *Langmuir*, 29(21):6201–6212. (Cited on page 6.)

Shyam, S., Asfer, M., Mehta, B., Mondal, P. K., and Almutairi, Z. A. (2020). Magnetic field driven actuation of sessile ferrofluid droplets in the presence of a time dependent magnetic field. *Colloids and Surfaces A: Physicochemical and Engineering Aspects*, 586:124116. (Cited on page 3.)

Sierou, A. and Brady, J. F. (2002). Rheology and microstructure in concentrated noncolloidal suspensions. *Journal of Rheology*, 46(5):1031–1056. (Cited on page 5.)

Srivastava, P., Malipeddi, A. R., and Sarkar, K. (2016). Steady shear rheology of a viscous emulsion in the presence of finite inertia at moderate volume fractions: sign reversal of normal stress differences. *Journal of Fluid Mechanics*, 805:494–522. (Cited on page 6.)

Sun, M., Yang, S., Jiang, J., and Zhang, L. (2023). Horizontal and vertical coalescent microrobotic collectives using ferrofluid droplets. *Advanced Materials*, 35(23):2300521. (Cited on page 1.)

Sussman, M., Smereka, P., and Osher, S. (1994). A level set approach for computing solutions to incompressible two-phase flow. *Journal of Computational physics*, 114(1):146–159. (Cited on page 18.)

Tan, S. H. and Nguyen, N.-T. (2011). Generation and manipulation of monodispersed ferrofluid emulsions: The effect of a uniform magnetic field in flow-focusing and T-junction configurations. *Physical Review E*, 84(3):036317. (Cited on page 2.)

Tan, S.-H., Nguyen, N.-T., Yobas, L., and Kang, T. G. (2010). Formation and manipulation of ferrofluid droplets at a microfluidic T-junction. *Journal of Micromechanics and Microengineering*, 20(4):045004. (Cited on page 2.)

Taylor, G. I. (1932). The viscosity of a fluid containing small drops of another fluid. *Proceedings of the Royal Society of London. Series A, Containing Papers of a Mathematical and Physical Character*, 138(834):41–48. (Cited on page 5.)

Taylor, G. I. (1934). The formation of emulsions in definable fields of flow. *Proceedings of the Royal Society of London. Series A, containing papers of a mathematical and physical character*, 146(858):501–523. (Cited on page 6.)

Teh, S.-Y., Lin, R., Hung, L.-H., and Lee, A. P. (2008). Droplet microfluidics. *Lab on a Chip*, 8(2):198–220. (Cited on page 2.)

Tryggvason, G., Scardovelli, R., and Zaleski, S. (2011). *Direct numerical simulations of gas–liquid multiphase flows*. Cambridge university press. (Cited on page 10.)

Wong, V.-L., Loizou, K., Lau, P.-L., Graham, R. S., and Hewakandamby, B. N. (2017). Numerical studies of shear-thinning droplet formation in a microfluidic t-junction using two-phase level-set method. *Chemical Engineering Science*, 174:157–173. (Cited on page 18.)

Wu, K. and Yao, Y. (1999). Dynamic structure study of fe3o4 ferrofluid emulsion in magnetic field. *Journal of magnetism and magnetic materials*, 201(1-3):186–190. (Cited on page 7.)

Xu, J.-J., Li, Z., Lowengrub, J., and Zhao, H. (2006). A level-set method for interfacial flows with surfactant. *Journal of Computational Physics*, 212(2):590–616. (Cited on page 18.)

Yang, H., Park, C. C., Hu, Y. T., and Leal, L. G. (2001). The coalescence of two equal-sized drops in a two-dimensional linear flow. *Physics of Fluids*, 13(5):1087–1106. (Cited on page 6.)

Zinchenko, A. (1984). Effect of hydrodynamic interactions between the particles on the rheological properties of dilute emulsions. *Journal of Applied Mathematics and Mechanics*, 48(2):198–206. (Cited on pages v, 38, and 39.)

Zinchenko, A. Z. and Davis, R. H. (2002). Shear flow of highly concentrated emulsions of deformable drops by numerical simulations. *Journal of Fluid Mechanics*, 455:21–61. (Cited on page 6.)